Summer 2017

A Study of Copper and Aluminum Incorporated Chromium Oxide Core-Shell Magnetic Nanoparticles

Tamzid Ibn Minhaj
Missouri State University, Tamzid7@live.missouristate.edu

A STUDY OF COPPER AND ALUMINUM INCORPORATED CHROMIUM OXIDE CORE-SHELL MAGNETIC NANOPARTICLES

A Masters Thesis

Presented to

The Graduate College of

Missouri State University

In Partial Fulfillment

Of the Requirements for the Degree

Masters of Science, Materials Science

By

Tamzid Ibn Minhaj

August 2017

A STUDY OF COPPER AND ALUMINUM INCORPORATED CHROMIUM OXIDE CORE-SHELL MAGNETIC NANOPARTICLES

Physics, Astronomy and Materials Science

Missouri State University, August 2017

Master of Science

Tamzid Ibn Minhaj

ABSTRACT

The structural and magnetic properties of copper (Cu) and aluminum (Al) -incorporated chromium oxide (α-Cr_2O_3, i.e., chromia) inverted core-shell nanoparticles (CSNs) were investigated. The objectives of this study were to determine the role of the substituting (for chromium, Cr) element and of Cu concentration on governing the magnetic properties of the CSNs. For synthesis of the CSNs, α-Cr_2O_3 nanoparticles were first grown using microwave assisted synthesis whereupon a hydrothermal nanophase epitaxy (HNE) method was used to incorporate Cu or Al in the chromia-based shell of the nanoparticles. The morphology, structure and size characteristics of the CSNs were determined using transmission emission microscopy (TEM) and x-ray diffraction (XRD). Rietveld refinement of the XRD data confirms continuation of corundum type structure throughout both core and shell. The high resolution (HR) TEM images confirmed the formation of distinct core and shell regions. The analysis of HR XPS (High resolution X-ray photoelectron spectroscopy) data confirmed the oxidation states of Cr, Cu and Al to be 3+, 2+ and 3+ respectively. Magnetic characterization shows that the Cu- and Al-substituted chromia-based CSNs of comparable concentration exhibit AFM-FM/FiM and predominantly AFM magnetic properties, respectively. The exchange bias properties were found to be optimized at a concentration of 3.92 atomic percentages (at%) in relation to lower and higher at% Cu substitution in the chromia-based CSNs.

KEYWORDS: core shell nano-particles, magnetic, hysteresis, exchange bias, coercivity

This abstract is approved as to form and content

_____

Robert A. Mayanovic, PhD
Chairperson, Advisory Committee
Missouri State University

A STUDY OF COPPER AND ALUMINUM INCORPORATTED

CHROMIUM OXIDE CORE-SHELL MAGNETIC NANOPARTICLES

By

Tamzid Ibn Minhaj

A Masters Thesis
Submitted to the Graduate College
Of Missouri State University
In Partial Fulfillment of the Requirements
For the Degree of Master of Science, Materials Science

August 2017

Approved:

_____
Robert A. Mayanovic, PhD

_____
Ridwan Sakidja, PhD

_____
Fei Wang, PhD

_____
Julie Masterson, PhD: Dean, Graduate College

ACKNOWLEDGEMENTS

First, I would like to thank Dr. Robert A. Mayanovic for being my thesis supervisor and guiding me throughout all the way. I would also like to thank Dr. Ridwan Sakidja (my computational guru) and Dr Kartik Ghosh – faculties PAMS, Md. Delower Hossain- former graduate student for their frequent cordial help in terms of instrument, software knowledge and conceptual assistance. I am very grateful to Mr. Rishi Patel of Jordan Valley Innovation Center (JVIC) for his patient help with x-ray photoelectron spectroscopy (XPS) measurements. It would be wrong not to thank Dr. Mourad Benamara – Director, Institute of Nanoscience and Engineering at University of Arkansas, Fayetteville for his help with Transmission Electron Microscope (TEM) images. I am thankful to all graduate students and stuff of PAMS department for creating such a nice, friendly and supportive environment.

Finally, I am thankful to my friend Ms. Greta M. Rueschmann for her excellent support throughout the whole writing process of this thesis.

I dedicate this thesis to my parents Gulshan Ara Begum and Md. Minhaj Uddin.

TABLE OF CONTENTS

LIST OF TABLES

LIST OF FIGURES

CHAPTER 1: INTRODUCTION

The magnetic core-shell nanoparticles (CSNs) are a very promising class of nanomaterials. They have the potential to minimize the dimensions of modern data storage devices. Their other principal potential applications include drug delivery, cancer treatment, magnetic resonance imaging (MRI), microwave absorption, and spintronic devices, and magnetic storage devices. In recent times, they have attracted renewed attention due to their previously unexplored potential which is becoming more accessible because of the development of new synthesis routes[1].

The core-shell structure most typically consists of different crystalline phases and/or compositions between the core and shell regions of the core-shell nanoparticle (NP) system. In reference to magnetic NPs, several research groups have studied different combinations of magnetic natures for core and shell. The systems having ferro/ ferrimagnetic (FM/FiM) core and antiferromagnetic (AFM) shells are known as regular core-shell (CS) magnetic systems as opposed to the systems having an AFM core and FM/FiM shells which are termed inverse CS systems or CSNs. Previous studies have also investigated systems of magnetically soft core, hard shell and vice versa. The initial development of research related to core shell structure in magnetic nanoparticles was driven by the attempt to avoid clustering and agglomeration which is undesirable for most of the applications. For this, primarily, non-magnetic shell regions were formed around magnetic nanoparticles[2]. The studies of these systems showed that interaction of core and shell can give rise to novel properties like exchange bias, which led to more

detailed studies on the effect of core-shell interaction realizing that this can be utilized for the customization of magnetic properties of CSNs.

The primary synthesis process for magnetic nanoparticles involves wet chemical methods. Processes like sol gel, co-precipitation and others, have been widely used. More recently, a dry chemical method called surface modification has been devised. Oxidation of a transition metal NP at the surface to forming a passive layer was one of the most common trends in this field. Surface reduction using carbon or hydrogen was also implemented. Although the simplicity and potential of the surface modification triggered a lot of interest, it was somewhat limited in terms of the choices of materials for core and shell. Also, the structure of core and shell is typically different using such methods, leading to substantial structural disorder at the core-shell interface.

Recently, developments in inorganic chemical synthesis methods have broadened the choice for core and shell materials in designing novel magnetic CSNs. Some general methods widely used for the synthesis of magnetic CSNs are seeded growth methods, surface treatment, ion substitution, co-precipitation, microwave irradiation, self-assembly etc. [1]

In most cases, the methods which are easy and inexpensive (e.g., surface treatment or surface modification) are limited in terms of their choice of possible combination. On the other hand, the comparatively complex and expensive methods offer great versatility. Therefore, the balance between these two is crucial for any study regarding magnetic CSNs.

However, when a combination of materials, which have different magnetic properties, are arranged in a nanoparticle system, this typically results in novel

characteristics in these systems which depend on the chemical nature of core and shell, shell thickness, defect concentration along the interface, anion and/or cation vacancies in the shell region, particle size of core and shell regions, etc. Exchange bias was first discovered in a core-shell nanoparticle (20 nm) system consisting of a Co core and a CoO shell. Meiklejohn and Bean[3] were first to report a special kind of magnetic anisotropy where Co/CoO CSNs shows a preference to magnetization in a particular direction.

The exchange bias effect manifests itself in bi-magnetic CSNs, magnetic multi-layer thin films, core-shell nanocrystallites, embedded nanoparticles, etc. Although much is known about the exchange bias, it is still under active investigation today. Undoubtedly, it is an interface event exhibited by systems that consist of an AFM material and a FM/FiM material in close proximity with respect to each other. It manifests itself in horizontal and sometimes vertical shifts of the hysteresis loops measured at field cooled condition (FC) with respect to zero field cooled (ZFC) condition. When an interfaced system of AFM and FM/FiM material layer is cooled in the ZFC condition below the Néel temperature (T_N), the AFM spin pairs freeze in a condition where the spins are aligned in every possible direction. As the external magnetic field (H) is varied, the spins at the interface in the FM/FiM layer become aligned in the direction of applied field. Therefore, ZFC case produces a hysteresis loop which is typically well centered both along the magnetic field (H) and the magnetization (M) axes. On the other hand, when the same system is cooled under the influence of a strong magnetic field below T_N, the surface spins of the AFM material freeze aligned in the direction of the applied field. This time, when measured, the hysteresis loop undergoes a shift (only horizontal or only vertical or both). The parallel surface spins of

the FM/FiM layer and the AFM layer interact with each other, which is known as the exchange interaction, causing them to align. When the external field attempts to flip the spins of the FM/FiM layer in the opposite (negative field) direction, it takes more energy to do so than in the ZFC condition. However, the direction of the spins of the AFM layer remains unchanged. And due to this, when the external field attempts to flip the direction of the FiM spins again in the (positive field) direction of the AFM spins, the flipping takes less energy. Due to this same exchange interaction, more FM/FiM spins remain aligned in the direction of AFM surface spins even if the applied field is zero. Conversely, fewer FM/FiM spins remain aligned after the external field is reduced to zero when initially they were aligned in the opposite direction of the AFM spins. This explains the vertical shift (along M) of the hysteresis loop due to the exchange interaction. Hysteresis loops in field cooled (FC) and zero field cooled (ZFC) conditions for a core shell structure having FM shell and AFM core with corresponding spin conditions are shown in Figure 1.1.

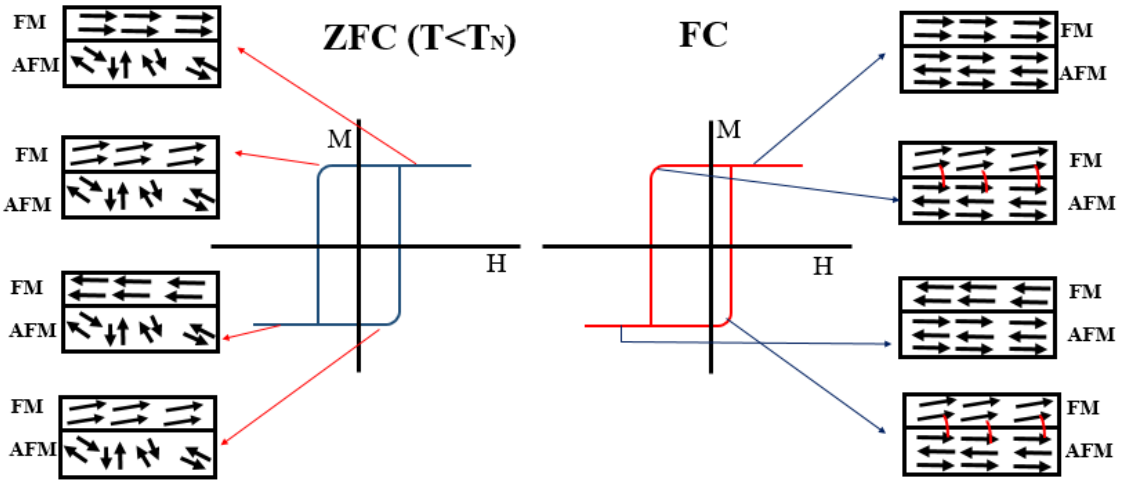

Figure 1.1: Hysteresis loops in field cooled (FC) and zero field cooled (ZFC) conditions.

While the exchange bias effect is typically sourced from different uncompensated surface spins, surface defects and spin-glass type spins, these are extremely hard to control and customize to put into use. The exchange bias derived from FM/FiM and AFM arranged layers has significant potential due to the controllability that can be manipulated for the sake of making devices.

Previous studies have explored various systems of hard/soft core/shell magnetic nanoparticle systems. These include Co/CoO, Fe/FeO, Ni/NiO etc. core-shell nanostructures. The inverse soft/hard nanosystems have also been studied. This includes, $FeCo/CoFe_2O_4$, $FeCoB/CoFeO_4$ and $FeCo(Al)/FeCo(Al)O_x$.

Chromium oxide is a very promising material due to its varied properties and suitability for numerous applications. The α-Cr_2O_3 has a hexagonal structure and one of the most stable oxides of chromium. It has a Néel temperature of 307 K[4] when measured in bulk material (this varies slightly with nanoparticle dimension). The Néel temperature is a temperature under which an antiferromagnetic material behaves as AFM and above which it becomes paramagnetic. It may conceptually be thought as parallel to the concept of a Curie temperature for ferromagnetic materials.

Chromium oxide, Cr_2O_3 has traditionally been used as green pigment, the performance of which is tunable for modern applications through different engineering techniques[5]. Historically, Cr_2O_3 is responsible for the hard corrosion resistant passive coating over stainless steel. Due to its high hardness, low friction coefficient and high thermal stability,[6] Cr_2O_3 has been used as a coating material, in digital recording systems,[7] etc. One of the most important features for any promising material is its tunability. Studies have shown that the property of the Cr_2O_3 as a protective coating can

be further enhanced by incorporating inorganic fullerene like tungsten disulfide, WS_2 nano-particles[7] for advanced applications.

Catalysts are widely used in industry to accelerate the rate of different important reactions which are naturally slow and bound by several equilibrium parameters. Traditionally, transition metal oxides are known to have catalytic property as a common feature. It has been shown by researchers that Cr_2O_3 has excellent catalytic action for ethylene and propylene polymerization[8]. Also, Cr_2O_3 supported on MCM-41 is an excellent catalyst for ethane dehydrogenation[9].

Designing materials with improved efficiency for photo thermal conversion of solar energy is one of the biggest challenges in the renewable energy sector. For this, materials with high absorption in the visible region and having high temperature stability is required. α-Cr_2O_3 has a bulk band gap of 3.2 eV and absorbs radiation just outside the visible region. V. Teixeira et al.[10] has reported a study where they have found that spectrally selective coating of Cr-Cr_2O_3 alternate layer demonstrates high absorption efficiency.

Also, due to the development of antibacterial resistance; research to fight new ways against bacterial infection has found renewed attention amongst medical community. Rakesh et. al.[11] has shown that Cr_2O_3 NP demonstrates promising antibacterial action against Escherichia coli and *Pseudomonas aregunosa*. Also it has proved to have no carcinogenic or poisonous action on physiology of mammals[12]. As a result, Cr_2O_3 NPs have great potential to be used as antibacterial agent in upcoming days.

Furthermore, chromium oxide has potential application in manufacturing spintronic devices. The spintronic devices are next generation electronic devices where

the fourth quantum state, the spin of an electron is manipulated to store and process data. They are promising because of being more size efficient, energy efficient and faster than conventional magnetic storage devices[13]. He et. Al.[13] reported a first principles computational study, where they have obtained a tunable reversible exchange bias by applied electric field in modified chromia single crystal at room temperature. The electric control of exchange bias is very critical for next generation spintronic devices. Hence, the study clearly proves the potential of Cr_2O_3 in spintronic device applications. However, understanding the concept of exchange bias is crucial for understanding the potential of chromium oxide based core-shell nanoparticles systems. Therefore, the exchange bias is one of the primary topics of this study. The principal motivation of this current study lies in earlier findings from studies made in our lab. In that series of studies, α-chromium oxide based CSNs were successfully made using transition elements iron, cobalt[14] , manganese and nickel[15]. The studies have shown clear evidence of formation of core shell nanostructure in all the systems mentioned above. The studies also demonstrated that the magnetic properties are quite tunable in terms of coercivity, exchange bias and remanence by controlling the modifying agents. Therefore, in order to provide completeness, it was important to investigate the effect of copper and aluminum addition to the α-Cr_2O_3 system.

One very important feature of this current study is investigation of the Cu concentration dependence on the structural and magnetic properties of the CSNs. Also, one of the principal questions that was addressed in this study is the following: is there an optimum level of Cu concentration for which the system possesses optimal magnetic properties. The study is divided into two parts. In the first part, the effect of aluminum

and copper addition in structure and properties of the α-Cr_2O_3 was investigated. Two separate batches of Cu and Al modified α-Cr_2O_3 CSNs were synthesized following a two-step process. The particle size was obtained from two different sources. First, the particle size was obtained using Scherrer formula. Then to verify the result, size distribution plots were obtained using low resolution transmission electron micrograph (LR-TEM) images. For further detailed structural analysis, a combination of high resolution transmission electron microscopy (HR TEM), electron dispersive spectroscopy (EDS), x-ray diffraction (XRD) and x-ray photoelectron spectroscopy (XPS) was utilized. Super conducting quantum interface device (SQUID) magnetometry was utilized to obtain hysteresis (Magnetization, M Vs Field, H) data both at field cooled (FC) and zero field cooled (ZFC) conditions.

In the second part, the study on copper ion concentration dependency of structure and magnetic properties of the CSNs system was carried out. For this, three batches of CSNs having 4.14 atomic percentages (at%), 4.28 at% and 5.71 at% copper were synthesized. During synthesis, all parameters were kept the same except the concentration of the Cu^{2+} containing solutions. Again, the size and morphology was verified using XRD and LR-TEM images. Structural characterization was performed using HR-TEM, XRD, EDX and XPS. Magnetic characterization of the CSNs was made using vibrating sample magnetometry (VSM).

CHAPTER 2: STUDY OF COPPER AND ALUMINUM MODIFIED CORE-SHELL NANOPARTICLES

Abstract

Due to the fact that their magnetic properties are quite tunable, magnetic core shell nanoparticles (CSNs) have become established as one of the most promising class of nanomaterials for magnetic and medicinal applications. They have a wide range of potential applications including but not limited to spintronic devices, spin valves, magnetic recording media, and cancer treatment (using hyperthermia). However, the search for optimum core-shell (CS) configurations for at or above room-temperature applications is still ongoing. Here we present a synthesis and characterization study of two different variations of CS chromium oxide nanoparticles (NPs). Corundum-structured α-Cr_2O_3 is antiferromagnetic (AFM) at room temperature (T_N~307 K) which provides an opportunity of using this material for spintronic devices by integrating/introducing a ferromagnetic (FM) or ferrimagnetic (FiM) shell on top of a AFM core. A two-step synthesis process was employed to synthesize the CSNs. First, a microwave assisted chemical synthesis route was used for growing pure α-Cr_2O_3 NPs. Subsequently our hydrothermal nanophase epitaxy (HNE) technique was employed for epitaxial deposition of either an Al- or Cu-incorporated chromia shell on a α-Cr_2O_3 core. Detailed structural, morphological, elemental and electronic characterization was made of our CSNs using XRD, TEM, SEM and XPS techniques. In addition, a SQUID magnetometer was used to determine the magnetic properties of our CSNs. Our XRD data demonstrate that the corundum structure has been maintained both in the core and

shell of our CSNs. The size obtained using the Scherrer formula is 27.55 nm, 36.45 nm and 37.5 nm for α-Cr_2O_3, α-Cr_2O_3@α-$Cu_xCr_{2-x}O_{3-y}$ and α-Cr_2O_3@α-$Al_xCr_{2-x}O_{3-y}$ respectively. X-ray photoelectron spectroscopy (XPS) confirmed the presence of 2.28 at% Cu in α-Cr_2O_3@α-$Cu_xCr_{2-x}O_{3-y}$ and 10.7 at% Al in α-Cr_2O_3@α-$Al_xCr_{2-x}O_{3-y}$ CSNs. The magnetic measurements have shown predominantly antiferromagnetic (AFM) behavior with presence of exchange bias (EB) in the field cooled vs zero field cooled hysteresis curves. The EB field values at 5 K are 163.2 Oe and 462.6 Oe for α-Cr_2O_3@α-$Cu_xCr_{2-x}O_{3-y}$ and α-Cr_2O_3@α-$Al_xCr_{2-x}O_{3-y}$, respectively.

Introduction

In order to scale existing spintronic and magnetic devices to the nano level, the attention of the scientific community has shifted from concentrating on thin-film based devices to investigation of nanostructured magnetic material systems. The exchange bias effect, which is exhibited by FM/AFM and FiM/AFM systems, is typically manifested by a hysteresis loop shift and, in some cases, by an enhanced coercive field. The anisotropy created by the exchange bias phenomenon is broadly attributed to the fact that the interface spins of the FM/FiM layer are induced to align themselves parallel to the spins of an adjacent AFM layer. This leads to a preferential directionality in spin alignment of the FM/FiM layer, which requires added energy by the applied field to flip the interface spins. Thus, the exchange bias effect leads to reduced volatility, which is a highly desirable property for magnetic storage device application[1].

However, efforts to establish precise control over the exchange bias effect in nanostructured systems are ongoing. Magnetic core-shell nanoparticles (CSNs), which

typically have a shell possessing a different magnetic structure than the core, have been shown to be promising for nanostructured magnetic systems applications. Research shows that the extent of exchange bias can be tuned by tailoring the composition, shape, size and atomic structure of the interface between the core and shell of CSNs[2]. In our previous work, we discovered that CSN formation using α-Cr_2O_3 as the core and incorporating cations such as Ni, Fe, and Co (M) in the outer chromia-based shell leads to the development of a ferromagnetic/ferrimagnetic character in the α-$M_xCr_{2-x}O_3$ nanophase. Magnetic characterization of our inverse α-Cr_2O_3@α-$M_xCr_{2-x}O_3$ AFM-FM/FiM CSNs has shown that they exhibit an appreciably strong exchange bias between the core and shell [3] . In continuation of that study, the search for potential candidate elements to be tested by incorporating them in the shell structure of α-Cr_2O_3 is ongoing.

Hammad et al.[4] reported room temperature ferromagnetic character in Cu^{2+}-modified zinc oxide nanoparticles. Substituting for Cr^{3+} ions with Cu^{2+} ions in the lattice will theoretically lead to a modification of band the band electronic band gap of the material. In addition, such substitution will most likely lead to an increase in the number of oxygen vacancies, which may have a bearing on the magnetic, electronic, and catalytic properties of the material. On the other hand, to the best of our knowledge, there are no studies that have investigated the effect of Al^{3+} incorporation in α-Cr_2O_3 system. Because Al is a row III element and Cr is row V element, substituting for Cr^{3+} with Al^{3+} has the potential to modify the local charge density distribution and thus alter the magnetic as well as optical characteristics of a new phase α-$M_xCr_{2-x}O_3$. The extent of physical property modification should vary depending on the concentration of the substituting species. We chose α-Cr_2O_3 as the core because this enables the formation of inverse bi-

magnetic CSNs having an AFM core and FM/FiM shell. Although, α-Cr_2O_3 has found widespread applications as green coloring agent[5], polishing and abrasive agent, protective coating[6-7], heterogeneous catalyst[8], antibacterial agent[9] and solar energy collector[10], the combination of room temperature AFM and magnetoelectric[11] properties makes α-Cr_2O_3 a highly potential candidate to be a component of a system exhibiting exchange bias.

The present study is concentrated on investigating the effect of introducing two distinct chemical species namely Cu^{2+} and Al^{3+}, separately in the α-Cr_2O_3 corundum structure. At the onset, α-Cr_2O_3 was synthesized using a microwave assisted method manipulating triethanolamine as a template[12].In the subsequent step, the hydrothermal nanophase epitaxy (HNE) method was adopted to modify the corundum structured α-Cr_2O_3[3]. After successful synthesis, the characterization was performed using XRD, SEM-EDS, TEM and XPS. A superconducting quantum interference device (SQUID) magnetometer was used to perform the magnetic measurements.

Experimental

Preparation of the CSNs. The preparation of CSNs was performed in a two-step process. In the first step, α-Cr_2O_3 nanoparticles were synthesized and in the next step the shell was formed on top of it. To grow α-Cr_2O_3, we followed the microwave irradiation assisted process described in Farzaneh et al.[12]. In this process, commercially available triethanolamine (TEOA), $C_6H_{15}NO_3$ was used as a template. Then, chromium (III) nitrate nonahydrate, $Cr(NO_3)_3.9H_2O$ solution was added with $C_6H_{15}NO_3$ and put through at least five cycles of magnetic stirring and heating. The speed for stirring was 8 rev/second and the microwave power was used up to 80 percent of maximum intensity. After completion

of the reaction (denoted by a gradual color change from pale green to blue green), the solution was mildly heated on a hot plate under a fume hood until it converted into a thick slurry. In the next step, it was calcined in a muffle furnace at 750^{o}C in excess air for 4 hours to obtain α-Cr_2O_3 nanoparticles. To form the core-shell nanostructure, we used the hydrothermal nanophase epitaxy (HNE) process developed in our lab as first described in a previous publication by Dey et al[3]. To synthesize α-Cr_2O_3@α-$Cu_xCr_{2-x}O_3$, a 10 mL of 0.05 M solution copper chloride ($CuCl_2$, Aldrich Chemical Company, Inc.) in deoxygenated (using N_2 stirring) warm deionized water (resistance 18.2 MΩ) was added with 0.33 gm of α-Cr_2O_3 nanoparticles. After half an hour of sonication, the solution was placed in an autoclave. The autoclave was loaded in a furnace and left there at 190^{o}C for 24 hours. In the next step, the solution was rinsed several times and then dried. The dry powders were then calcined at 450^{o}C for 5 hours in a forming gas (95% argon + 5% hydrogen) environment to synthesize α-Cr_2O_3@α-$Cu_xCr_{2-x}O_3$. Using the identical procedure, 0.05 M solution of aluminum chloride ($AlCl_3$) was used for growing α-Cr_2O_3@α-$Al_xCr_{2-x}O_3$ CSNs.

The model of the instrument used for scanning electron microscopy (SEM) and energy dispersive x-ray spectroscopy (EDX) is FEI Quanta 200. SEM images of the powdered samples were taken on carbon tape at 20 KV beam voltage. The imaging distance was kept at 6 mm and the gun-to-sample EDX distance was kept at 15 mm. A short piece of carbon tape was used as a bridge between the top face of the stage to the bottom portion of the stage to minimize charging effects. The SEM images of α-Cr_2O_3@α-$Cu_xCr_{2-x}O_3$ and α-Cr_2O_3@α-$Al_xCr_{2-x}O_3$ CSNs and corresponding EDX spectra are shown in Figure 2.1.

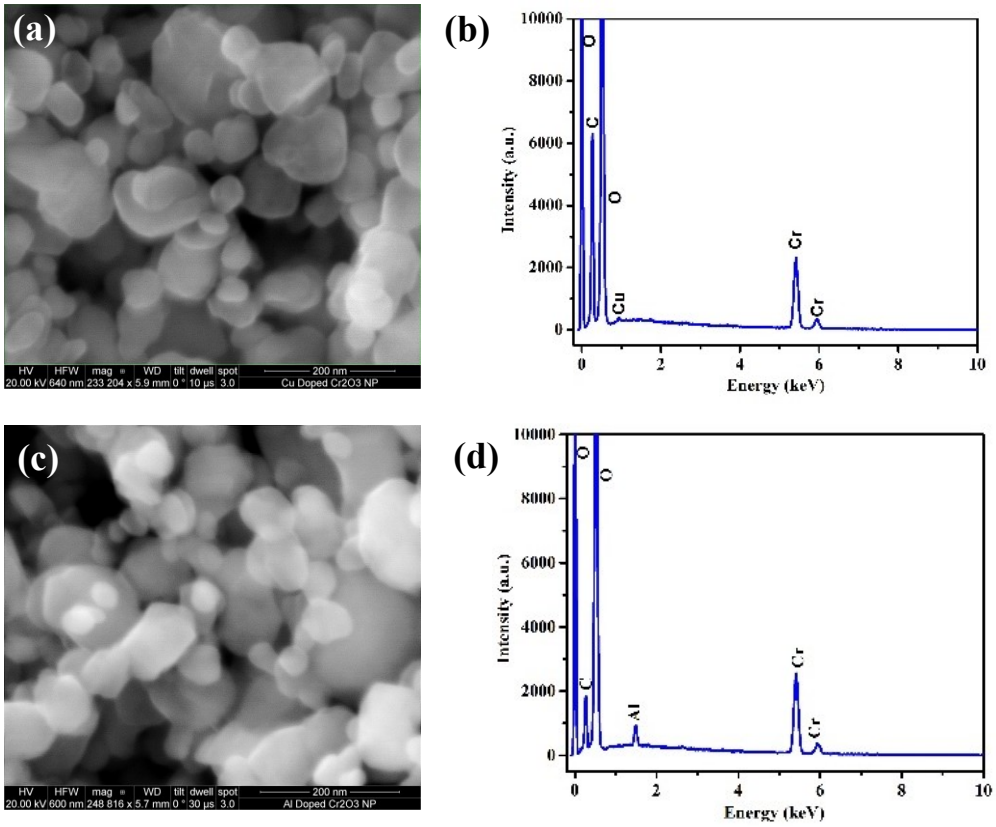

Figure 2.1: (a) SEM image of α-Cr_2O_3@α-$Cu_xCr_{2-x}O_3$ and (b) corresponding EDX spectra; (c) SEM image of α-Cr_2O_3@α-$Al_xCr_{2-x}O_3$ and (d) corresponding EDX spectra.

Transmission electron microscopy (TEM). The instrument used for TEM was an FEI Titan 80-300 Transmission Electron Microscope. The operation voltage of the TEM field emission gun was 300 keV. The ImageJ software was used to measure the particle sizes from three different low resolution TEM images and the distribution curve was plotted using Origin Pro software. In Figure 2.2(a) the low resolution TEM image of Cr_2O_3@α-$Cu_xCr_{2-x}O_3$ and in Figure 2(b) the corresponding particle distribution are shown. Figure 2.2(c) shows the low resolution TEM image of α-Cr2O_3@α-$Al_xCr_{2-x}O_3$ and Figure 2.2(d) shows the corresponding particle distribution. Table 2.1 shows the particle size analysis obtained from XRD data and LR-TEM images.

LR-TEM images of α-Cr_2O_3 particles (Figure S2.1) and corresponding particle

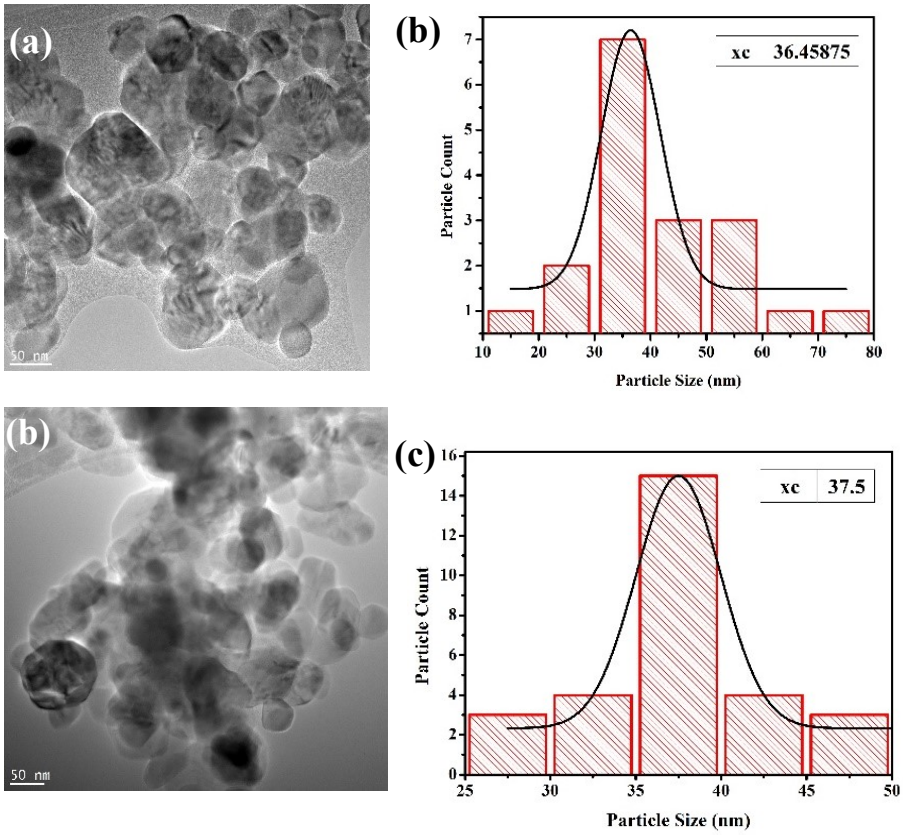

Figure 2.2: (a) Low resolution TEM image of α-Cr_2O_3@α-$Cu_xCr_{2-x}O_3$ and (b) corresponding size distribution of particles; (c) Low resolution TEM image of α-Cr_2O_3@α-$Al_xCr_{2-x}O_3$ and (d) corresponding size distribution of particles.

Table 2.1: Particle size obtained from XRD data and LR-TEM images

	Particle Size from XRD (nm)	**Particle Size from TEM (nm)**	**Sigma (nm)**	**FWHM**
α-Cr_2O_3	28.5	27.6	3.1	7.4
Cu-Cr_2O_3	33.2	36.5	5.3	12.5
Al-Cr_2O_3	38.3	37.5	2.2	5.3

distribution are attached in Appendix A. Figure 2.3(a) shows the HR-TEM image of an α-Cr_2O_3@α-$Cu_xCr_{2-x}O_3$ Figure 2.3(b) shows the magnified core shell region and Figure

2.3(c) and 2.3(d) shows the fast Fourier transform (FFT) of the corresponding core and shell regions.

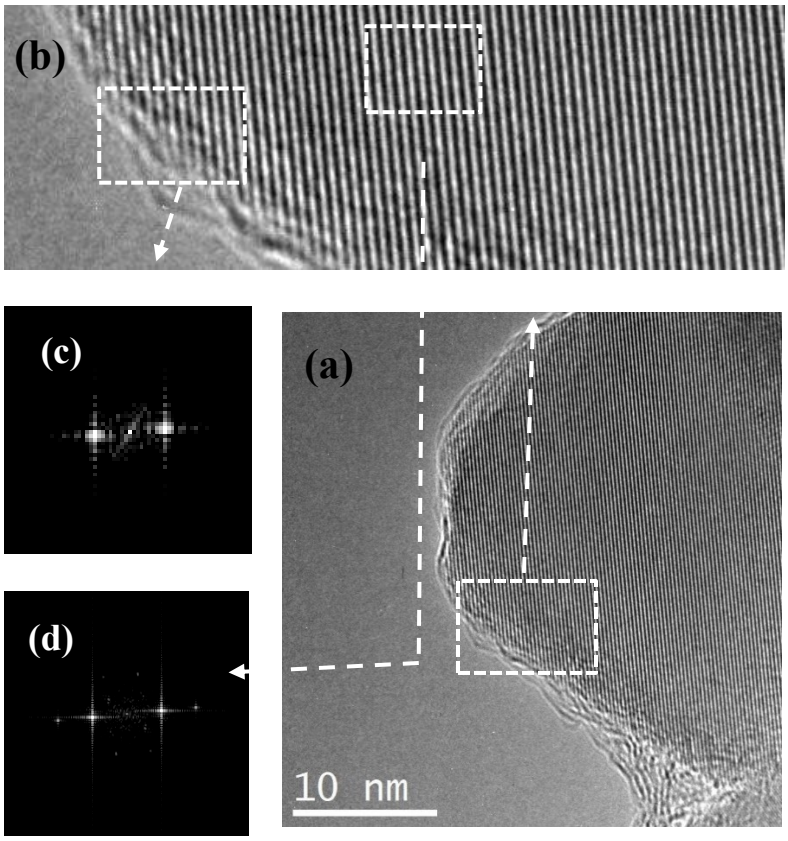

Figure 2.3: (a) HR-TEM image of a single α-Cr_2O_3@α-$Cu_xCr_{2-x}O_3$ particle, (b) magnified view of the core and shell region showing characteristic contrast, (c) Fast Fourier Transform (FFT) of shell region and (d) Fast Fourier Transform (FFT) of core region. of the core and shell regions. Figure 2.4(a) shows the HR-TEM image of an α-Cr_2O_3@α-$Al_xCr_{2-x}O_3$. Figure 2.4(b) shows the magnified core shell region.

X-Ray Photoelectron Spectroscopy (XPS). The XPS measurements were performed to confirm the composition of the CSNPs as well as to identify the oxidation states of the cation species. The instrument used for this purpose was a Thermo Scientific Alpha 110 hemispherical analyzer of 25 eV pass energy. For the x-ray source, an Al Kα irradiation of 1486.6 eV was used. The $Ag3d_{5/2}$ peak with characteristic energy of

368.26eV and FWHM of 0.36eV was used for the calibration of source and analyzer. The peak fitting

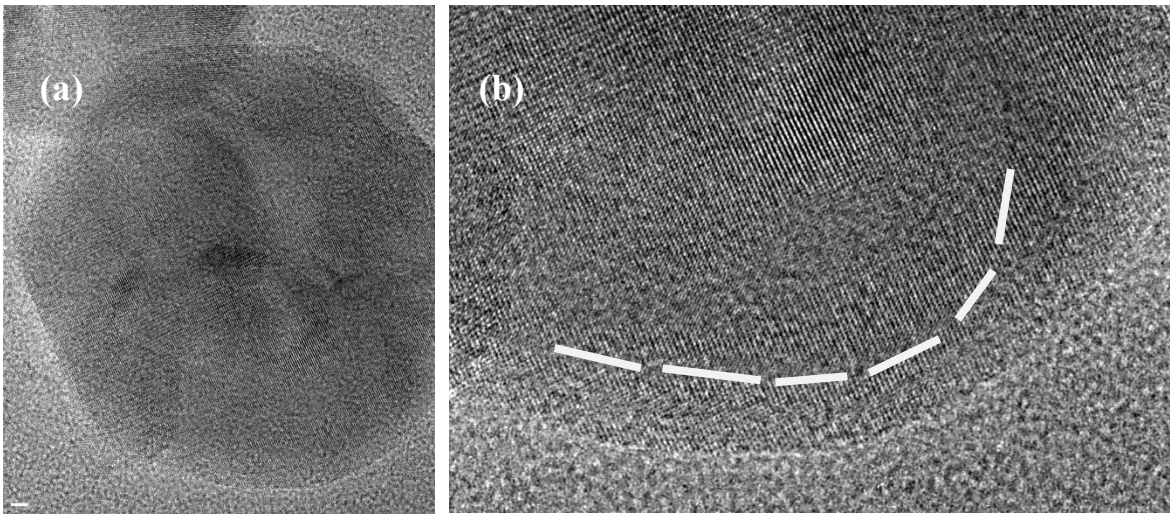

Figure 2.4: (a) HR-TEM image of a single α-Cr_2O_3@α-$Al_xCr_{2-x}O_3$ particle, (b) magnified view of the core and shell region showing characteristic contrast.

and analysis of the XPS data was made using the CasaXPS 2.3.16 software, where the carbon 1s peak (284.8 eV) from carbon tape on which the samples were spread was utilized for calibration.

The Shirley background function was used to model the background of the collected data. For peak fitting of high resolution data, two different types of fitting functions were used as per the nature of the peak. To fit symmetrical line shaped peaks, a GL (30) function was used. Here, GL is an acronym; where, G stands for Gaussian and L stands for Lorentzian. On the other hand, to fit asymmetric line shapes, a Lorentzian functional form convoluted with a Gaussian LA (a,b,n) function was used. The data obtained from XPS measurements of $Cu2p_{3/2}$ of α-Cr_2O_3@α-$Cu_xCr_{2-x}O_3$ are summarized

in Figure 2.5 and the data obtained from XPS measurements of $Cu2p_{3/2}$ of α-Cr_2O_3@α-$Al_xCr_{2-x}O_3$ are summarized in Figure 2.6.

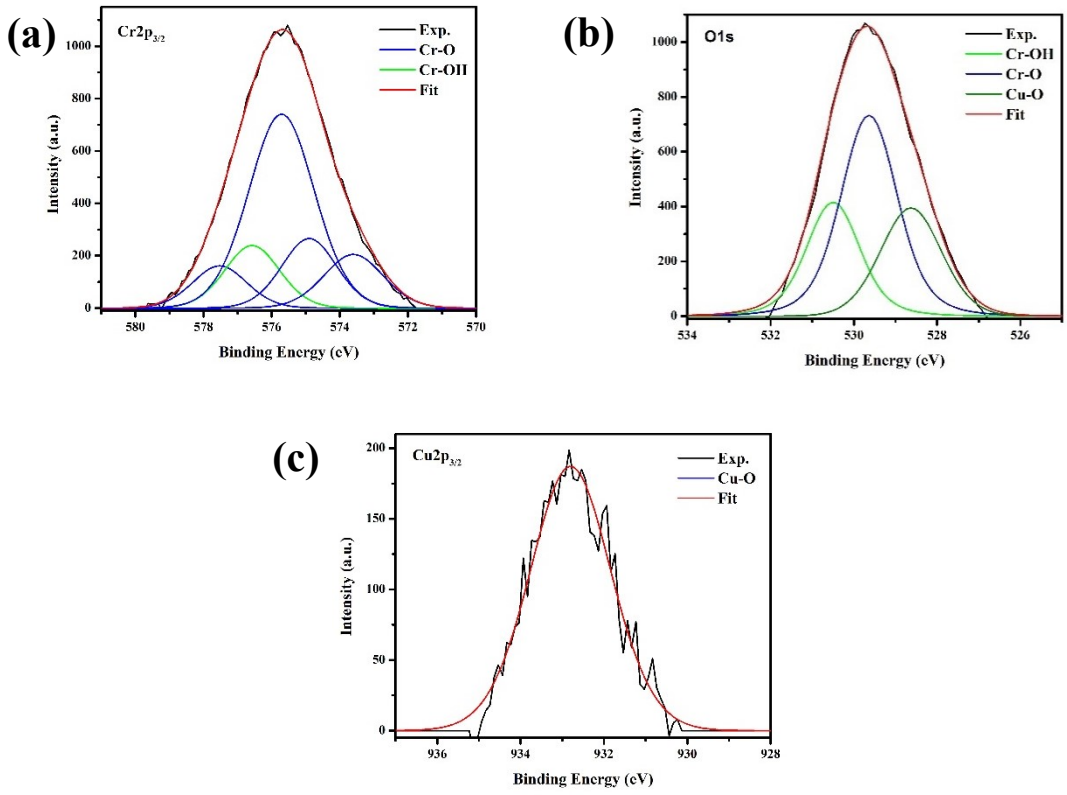

Figure 2.5: HR-XPS peaks of (a) $Cr2p_{3/2}$ and (b) O1s (c) $Cu2p_{3/2}$ of α-Cr_2O_3@α-$Cu_xCr_{2-x}O_3$

X-ray Diffraction (XRD). All x-ray diffraction (XRD) measurements were performed at room temperature. The instrument used for this purpose was a Bruker D-8 diffractometer. Powder samples were randomly dispersed in a thick layer on a glass slide; ethanol was used for the settling agent. The slide was placed on a vertical aluminum stage using double sided tape. A copper Kα irradiation of 1.54184 Å wavelength was used for which the source was operating at 40 kV and 40 mA. Two 0.6 mm slits were used in the

XRD instrument, one in the incident side and another in front of the detector. Also, a Göbel mirror was used in the incident side.

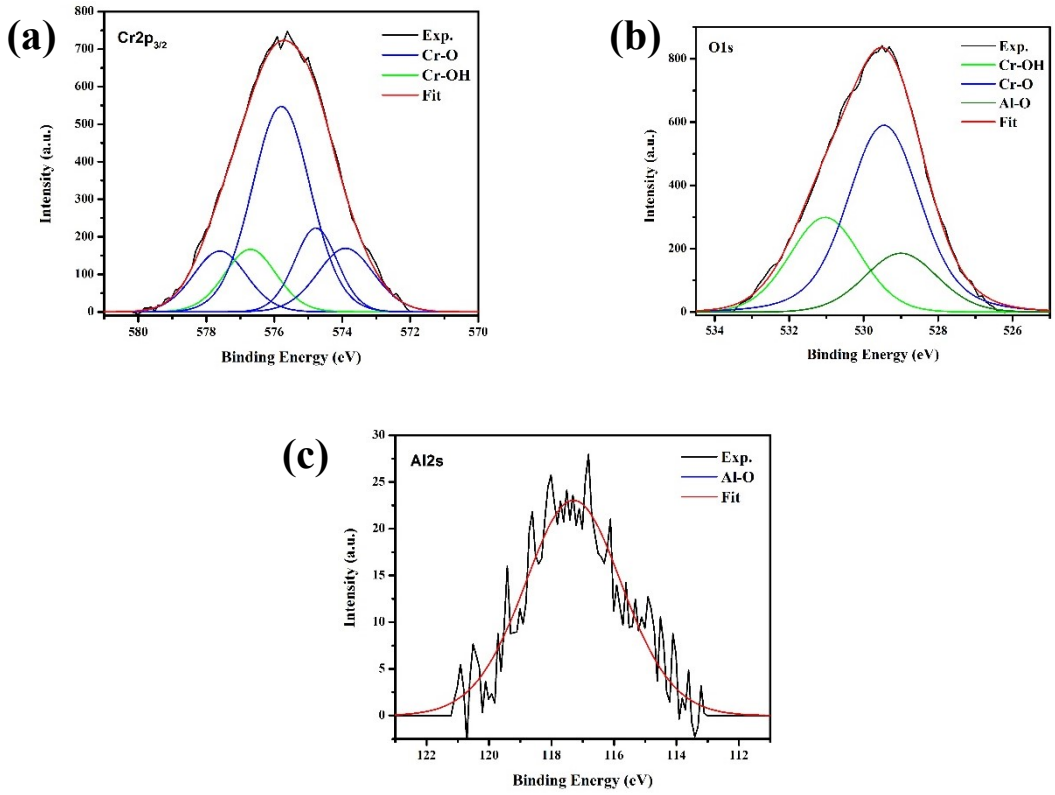

Figure 2.6: HR-XPS peak of (a) $Cr2p_{3/2}$ and (b) O1s (c) Al2s of α-Cr_2O_3@α-$Al_xCr_{2-x}O_3$

Two different analyses were performed on the XRD data to extract two separate sets of information. The first one used the Scherrer equation, which uses the spread of the peaks originating from different planes to obtain the particle size. The value of the shape constant used in this formula was assumed to be 0.9. In the second method, Rietveld refinement was used, which refines the lattice structure and structural parameters. A ninth order Chebychev polynomial was used to model the background function of obtained diffraction pattern. The fitted XRD data of α-Cr_2O_3@α-$Cu_xCr_{2-x}O_3$ and α-$Cr2O_3$@α-$Al_xCr_{2-x}O_3$ are presented in Figure 2.7(a) and 2.7(b).

Table 2.2 and 2.3 summarizes the structural information obtained after performing

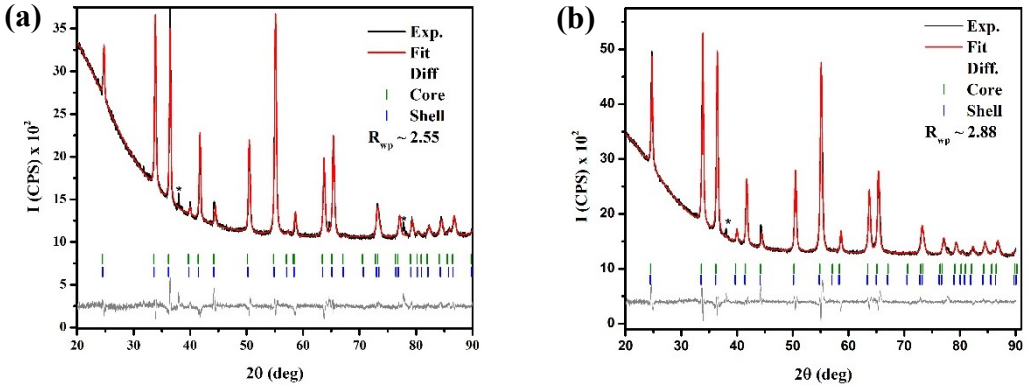

Figure 2.7: (a) The Rietveld refinement of XRD data of α-Cr_2O_3@α-$Cu_xCr_{2-x}O_3$ and (b) α-Cr_2O_3@α-$Al_xCr_{2-x}O_3$. The vertical marks show the Bragg angle position for core and shell (Here, * represents unidentified peaks)

Rietveld refinement of XRD data of α-Cr_2O_3@α-$Cu_xCr_{2-x}O_3$ and α-Cr_2O_3@α-$Al_xCr_{2-x}O_3$ CSNs respectively.

Table 2.2: Summary of structural information gathered through Rietveld refinement of XRD data of α-Cr_2O_3@α-$Cu_xCr_{2-x}O_3$ core-shell nano-particles

Core: α-Cr_2O_3 NPs					
	a (Å)	b (Å)	c (Å)	Volume (Å^3)	Core Size (nm)
	4.958	4.958	13.59	289.31	28.011
Atoms	x	y	z	Occupancy	Beq. (Å^2)
Cr	0	0	0.35180	1.0	0.6
O	0.29697	0	0.25	1.0	0.6

Shell: α-$Cu_xCr_{2-x}O_3$					
	a (Å)	b (Å)	c (Å)	Volume (Å^3)	Shell Size (nm)
	4.965	4.965	13.61	290.63	25.465
Atoms	x	y	z	Occupancy	Beq. (Å^2)
Cr	0	0	0.34221	0.90	0.5866
O	0.32146	0	0.25	0.96	0.1000
Cu	0	0	0.34499	0.10	0.1280

Table 2.3: Summary of structural information gathered through Rietveld refinement of XRD data of α-Cr_2O_3 /$Cu_{0.74}Cr_{1.26}O_{2.65}$ core-shell nanoparticles.

Core: α-Cr_2O_3 NPs					
	a (Å)	b (Å)	c (Å)	Volume (Å^3)	Core Size (nm)
	4.959	4.959	13.616	290.04	33.26
Atoms	x	y	z	Occupancy	Beq. (Å^2)
Cr	0	0	0.35180	1.0	1.18
O	0.27632	0	0.25	1.0	1.20

Shell: α-$Al_xCr_{2-x}O_3$					
	a (Å)	b (Å)	c (Å)	Volume (Å^3)	Shell Size (nm)
	4.958	4.958	13.58	289.104	36.289
Atoms	x	y	z	Occupancy	Beq. (Å^2)
Cr	0	0	0.34258	0.57	0.600
O	0.3394	0	0.25	1.00	1.199
Al	0	0	0.34304	0.43	0.600

The composition obtained from XPS analysis are tabulated in table 2.4. Table 2.5 summarizes the chemical formulas obtained for the CSNs by combination of XPS and XRD data. An example of the shell formula calculation for α-Cr_2O_3@α-$Cu_xCr_{2-x}O_3$ and the model of a CSN (Figure S2.2) used for the calculation are shown in appendix A.

Table 2.4: Chemical composition obtained from XPS analysis.

Sample	**Shell Thickness (nm)**	**At%**	**At% Chromium**	**At% Oxygen**
Cu- Cr_2O_3	4.0	2.3 (Cu)	39.2	58.5
Al- Cr_2O_3	4.5	10.7 (Al)	29.2	60.1

Table 2.5: Calculated chemical formulas for the shell of the modified CSNs

Sample No.	Molecular Formula
1	α-Cr_2O_3@$Cu_{0.19}Cr_{1.80}O_{2.87}$
2	α-Cr_2O_3@$Al_{0.86}Cr_{1.14}O_3$

Magnetic Measurements. A Quantum Design SQUID MPMS/XL magnetometer was used for the magnetic measurement of the CSNs. Hysteresis and M vs T measurements were performed in both field cooled (FC) and zero field cooled (ZFC) conditions. At first, a measured amount of NPs were placed in soft gel capsules which were loaded in the magnetometer. For FC hysteresis measurement, the temperature was first raised to 330 K and then a field of 20 kOe was applied. The temperature was then gradually lowered down to 5 K. The M vs H data were obtained in ±50 kOe range. For ZFC hysteresis measurement, the same cycle was followed but a zero field was applied during cooling from 330 to 5 K. During FC M vs T measurements, a 500 Oe field was applied while collecting data from 5 to 330 K. Figure 2.8 summarizes the results of magnetic measurement (hysteresis and M Vs T plots) of α-Cr_2O_3, α-Cr_2O_3@α-$Cu_xCr_{2-x}O_3$ and α-Cr_2O_3@α-$Al_xCr_{2-x}O_3$ NPs. The insets of the Figures shows the M Vs T values between 50-80 (Figure 2.8(d)) and 50-65 K (Figure 2.8 (e)).

Results and Discussion

Despite some agglomeration of the particles, the SEM images show the nanoparticles as having a faceted or pseudo spherical shape (Figure 2.1(a) and 2.1(c)).

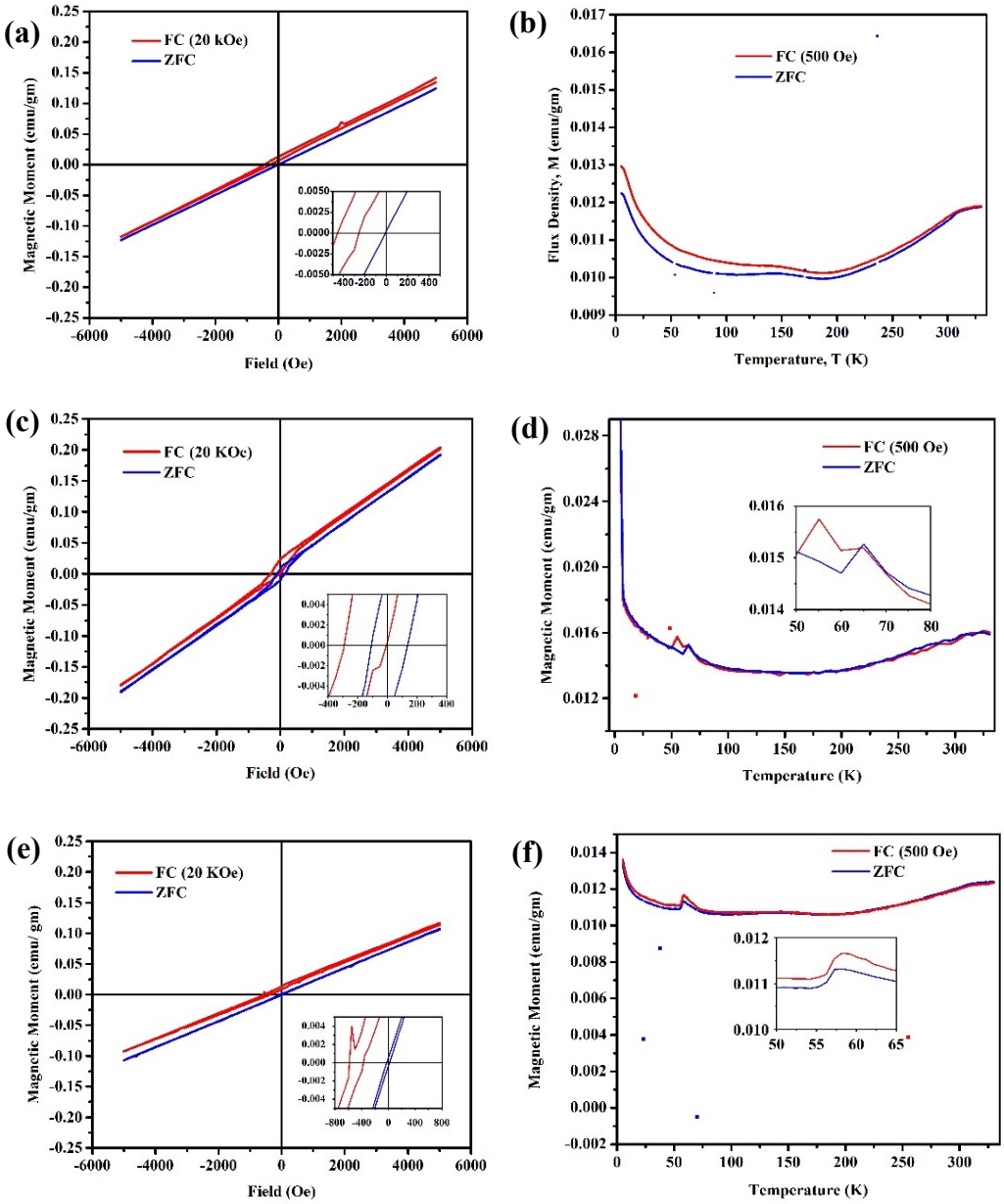

Figure 2.8: Field cooled (FC) and zero field cooled (ZFC) hysteresis loops of (a) α-Cr_2O_3 (c) α-Cr_2O_3@α-$Cu_xCr_{2-x}O_3$, (e) α-Cr_2O_3@α-$Al_xCr_{2-x}O_3$ measured at 5 K, and magnetization (M) versus temperature (T) plots of (b) α-Cr_2O_3 (d) α-Cr_2O_3@α-$Cu_xCr_{2-x}O_3$, (f) α-Cr_2O_3@α-$Al_xCr_{2-x}O_3$

The EDS spectra confirm the presence of the Cr, Cu or Al, and O elements and show that there are no impurity elements in the synthesized CSNs. In Figures 2.1(b) and 2.1(d), the carbon peaks are obtained from carbon tape used to hold the nanoparticles. For

obtaining a particle size distribution, the low resolution TEM images of Figure 2.2(a) and 2.2(c) were considered. To calculate the average particle size, the data were fitted using a Gaussian function. The size of the α-Cr_2O_3@α-$Cu_xCr_{2-x}O_3$ CSNs was found to be 36.45 nm and that of α-Cr_2O_3@α-$Al_xCr_{2-x}O_3$.The average size was determined to be 37.5 nm. The particle sizes were also determined from XRD data using Scherrer equation, which produced nearly identical values.

The XRD data were fitted assuming two different structure (cif) files: one for the core and the other for the shell. The shell file was formed by substitution for Cr^{+3} ions with either Cu^{+2} or Al^{+3} ions. For the shell of α-Cr_2O_3@α-$Cu_xCr_{1-x}O_3$ CSNs, the occupancy of Cr^{3+} was set to 0.9 and occupancy of Cu^{+2} was set to point 0.1. On the other hand, for the shell of α-Cr_2O_3@α-$Al_xCr_{1-x}O_3$, the occupancy of Cr^{3+} was set to 0.57 and occupancy of Al^{+3} was set to point 0.43. These occupancy values are set according to the calculated stoichiometric value obtained using TEM and HR-XPS data. An example of the calculation leading to the stoichiometry formula of the shell is included in supplementary information section of this paper. The tiny vertical lines in two different rows under the peaks in Figure 2.3(a) and 2.3(b) denote the Bragg angle positions for core vs shell fitting. According to Shannon,[13] the ionic radii of Cr^{+3}, Cu^{+2} and Al^{+3} are 0.73Å, 0.87Å and 0.535 Å respectively. Therefore, in cases where a Cr^{+3} gets substituted by a Cu^{+2}, a tensile stress field is expected to produce localized expansion of the lattice structure, which in effect is expected to change lattice spacing (d) values and shift Bragg angle (2θ) position to the lower values in α-Cr_2O_3@α-$Cu_xCr_{2-x}O_3$ compared to the original α-Cr_2O_3 structure. The exact opposite to this is expected to be observed in α-Cr_2O_3@α-$Al_xCr_{2-x}O_3$. The XRD data fitted using Rietveld refinement conformed to this

prediction, which indirectly verifies the formation of a core shell structure in the measured CSNs. Assuming a core shell structure provided a better fit than when a Rietveld refinement was attempted using single phase (as evidenced in higher R_{wp} values for the latter refinement).

The HR-TEM images of core and shell regions of α-Cr_2O_3@α-$Cu_xCr_{2-x}O_3$ are shown in Figure 2.4. Figure 2.4(a) shows the FFT of shell region and Figure 2.4(d) shows the FFT of the core region. Comparing the FFT of these two regions substantiates that these two regions have similar crystal structure. The high resolution (HR) XPS data confirmed that the α-Cr_2O_3@α-$Cu_xCr_{2-x}O_3$ CSNs contain 2.28 At% Cu and the α-Cr_2O_3@α-$Al_xCr_{2-x}O_3$ CSNs contain 10.7 At% Al. The analysis of the HR Cu2p peak confirmed that copper is in Cu^{2+} oxidation state and of the HR Al2p confirmed that Al is in Al^{+3} oxidation state.

The hysteresis data (M Vs H) for both FC and ZFC conditions at 5K are plotted in Figures 2.6(a) and 2.6(c). The total range of the measurement was – 5kOe to +5kOe. The hysteresis plots of α-Cr_2O_3@α-$Cu_xCr_{2-x}O_3$ (Figure 2.6(a)) demonstrate a weak FM/FiM behavior accompanied by an exchange bias of ~163.179 Oe and an enlargement in the net coercive value (from 99.66 Oe of α- Cr_2O_3 to 143.241 Oe). The net coercive field is defined as the absolute value of the difference of the coercive fields of ascending and descending curves of FC and ZFC measurements. On the other hand, the hysteresis plots of α-Cr_2O_3@ α-$Al_xCr_{2-x}O_3$ (Figure 2.6(b)) demonstrate an almost pure antiferromagnetic behavior accompanied by an exchange bias value of 462.6 Oe. The M Vs T plots for both FC and ZFC conditions of α-Cr_2O_3@α-$Cu_xCr_{2-x}O_3$ and α-Cr_2O_3@α-$Al_xCr_{2-x}O_3$ are shown in Figures 2.6(b) and 2.6(d) respectively. Both plots show a kinked feature starting at ~60

K. This phenomenon may be attributed to a frozen spin transition of a spin structure having similar characteristics, but not the same, as the canonical spin glass. This is only a conjecture and needs to be verified through further studies.

Conclusions

The attempt to incorporate Cu and Al in the α-Cr_2O_3 nanoparticle was successful. The TEM and XRD data collectively verify the formation of a core shell structure having a core of about 28 nm and shell of 4 and 4.5 nm for α-Cr_2O_3@α-$Cu_xCr_{2-x}O_3$ and α-Cr_2O_3@α-$Al_xCr_{2-x}O_3$, respectively. The magnetic measurements demonstrated weak exchange interaction between core and shell in both NP systems, the value of which were measured from shifting of FC hysteresis loop center from ZFC center (either vertical or horizontal). The Cu-chromia CSNs has shown weak ferrimagnetic behavior, whereas Al-Chromia has shown almost pure AFM characteristics.

References

1. Sort, J. *et al.* Exchange bias in nanostructures. *Phys. Rep.* **422,** 65–117 (2005).

2. Dimitriadis, V., Kechrakos, D., Chubykalo-Fesenko, O. & Tsiantos, V. Shape-dependent exchange bias effect in magnetic nanoparticles with core-shell morphology. *Phys. Rev. B* **92,** (2015).

3. Dey, S., Hossain, M. D., Mayanovic, R. A., Wirth, R. & Gordon, R. A. Novel highly ordered core–shell nanoparticles. *J. Mater. Sci.* **52,** 2066–2076 (2017).

4. Hammad, T. M., Salem, J. K., Harrison, R. G., Hempelmann, R. & Hejazy, N. K. Optical and magnetic properties of Cu-doped ZnO nanoparticles. *J. Mater. Sci. Mater. Electron.* **24,** 2846–2852 (2013).

5. Li, P. *et al.* The effects of Al and Ba on the colour performance of chromic oxide green pigment. *Dyes Pigments* **80,** 287–291 (2009).

6. Pang, X. *et al.* Investigation of microstructure and mechanical properties of multi-layer Cr/Cr_2O_3 coatings. *Thin Solid Films* **517,** 1922–1927 (2009).

7. Hou, X. & Choy, K.-L. Synthesis of Cr2O3-based nanocomposite coatings with incorporation of inorganic fullerene-like nanoparticles. *Thin Solid Films* **516,** 8620–8624 (2008).

8. Rao, T. V. M., Zahidi, E. M. & Sayari, A. Ethane dehydrogenation over pore-expanded mesoporous silica-supported chromium oxide: 2. catalytic properties and nature of active sites. *J. Mol. Catal. Chem.* **301,** 159–165 (2009).

9. Rakesh, Ananda, S. & Gowda, N. M. M. Synthesis of chromium(III) oxide nanoparticles by electrochemical method and Mukia Maderaspatana Plant Extract, characterization, $KMnO_4$ decomposition and antibacterial Study. *Mod. Res. Catal.* **02,** 127–135 (2013).

10. Teixeira, V. *et al.* Spectrally selective composite coatings of Cr–Cr_2O_3 and Mo–Al_2O_3 for solar energy applications. *Thin Solid Films* **392,** 320–326 (2001).

11. Fallarino, L., Berger, A. & Binek, C. Giant temperature dependence of the spin reversal field in magnetoelectric chromia. *Appl. Phys. Lett.* **104,** 022403 (2014).

12. Farzaneh, F. Synthesis and characterization of Cr_2O_3 nanoparticles with triethanolamine in water under microwave irradiation. *J. Sci. Islam. Repub. Iran* **22,** 329–333 (2011).

13. R. D. Shannon. Revised effective ionic radii and systematic studies of interatomic distances in halides and chalcogenides. (1976).

CHAPTER 3: THE EFFECT OF COPPER CONCENTRATION IN STRUCTURE AND MAGNETIC PROPERTIES OF MODIFIED CHROMIUM OXIDE CORE SHELL NANOPARTICLES

Abstract

In my previous study, I have shown that incorporating copper in the corundum structured α-Cr_2O_3 NPs gives rise to either ferro- or ferrimagnetic properties at low temperature (5 K). The purpose of this study was to obtain a greater understanding on the substituting species (i.e., copper) concentration dependency of the structure and magnetic properties of α-Cr_2O_3@α-$Cu_xCr_{2-x}O_3$ core-shell nanoparticles. In this study, I have used a hydrothermal nanophase epitaxy (HNE) method to grow three sets α-Cr_2O_3@α-$Cu_xCr_{2-x}O_3$ core-shell nanoparticles of variable copper concentration. The high-resolution x-ray photoelectron (HR- XPS) study shows that the concentration of the synthesized particles is 3.92 at%, 6.17 at% and 7.68 at%. The particle size was determined to be 35.5 nm, 32.5 nm and 34.5 nm by analysis of low resolution transmission electron micrograph images, which was further verified from analysis of the x-ray diffraction data. The bright field high resolution (HR) TEM images clearly show the core and shell regions of the CSNs. The x-ray diffraction (XRD) analysis has shown that the original corundum structure of α- Cr_2O_3 has been maintained in both core and shell regions. The high resolution XPS data have shown that chromium and copper of synthesized NPs are in +3 and +2 oxidation states respectively. The magnetic analysis performed using vibrating sample magnetometry (VSM) demonstrated clear dependency of coercivity (H_C), remanence (M_R) and exchange bias (both horizontal, H_{EB} and vertical, M_{EB}) on copper concentration.

Also, I have found weak ferrimagnetic (FiM) behavior in Cu-bearing chromium oxide CSNs at room temperature (300 K) which is a feat difficult to achieve in CSN systems. The value of coercivity, when measured at 10 K increased from 422 Oe to 457 Oe along with the variation of copper concentration from 3.92 at% to 6.17 at%. However, when the copper concentration was raised to 7.68 at%, the magnetic behavior changed back to antiferromagnetic (AFM) which can be hypothesized to be due to a saturation effect.

Introduction

Core-shell magnetic nanoparticles (CSNs) offer a broad spectrum of prospective applications. The research regarding this area gained renewed acceleration in the last few decades due to two principal reasons: the continuous drive by modern technologies for advanced materials with customized properties and precise control over structure of these systems which was made possible by recent development of synthesis routes in the field of inorganic chemistry[1].

The principal feature offered by CSN systems is their tunability. For magnetic CSNs, a wide variety of magnetic properties can be achieved depending on several structural parameters; for example- chemical composition and crystal structure of the core and shell, shell thickness, the concentration of defects along the interface, the particle size, etc. Often the electronic interaction between the core and shell along the interfacial region may give rise to novel properties such as exchange bias along with modification of existing properties (band gap expansion/contraction)[1].

Chromium oxide (α-Cr_2O_3) is the most stable oxide of the transition element chromium. It shows antiferromagnetic (AFM) behavior at room temperature. The Néel

temperature of bulk α- Cr_2O_3 is 307 K which varies slightly as the particle size approaches nano scale[2]. Another very interesting property of α- Cr_2O_3 is its magnetoelectric nature[3]. α-Cr_2O_3 is known for its application for protective coatings, digital recording systems[4], heterogeneous catalysis[5,6], as an anti-bacterial agent[7], and solar energy collection[8]. It has high potential for spintronic device application, due in part to its magnetoelectric effect, which is predicted by theoretical calculations[9].

The successful synthesis of transition metal (TM: Fe, Co, Ni, Mn) modified α-Cr_2O_3 CSNs were synthesized in our lab[10–12] using our hydrothermal nanophase epitaxy (HNE) method. The HNE has been demonstrated to produce better interface (less defects) region properties due to the epitaxial nature of shell growth[10–12]. The TM-substituted chromia based CSNs have shown significant shift of field cooled (FC) vs zero field cooled (ZFC) hysteresis loop measurements, which has been attributed to the exchange interaction along the interface region. Nevertheless, only α-Cr_2O_3@α-$Cu_xCr_{2-x}O_3$ CSNs have shown significant ferrimagnetic (FiM) ordering at room temperature. However, no concentration-dependent study has been performed thus far, which could be significant for both developing a better understanding of the magnetic properties of TM-substituted chromia based CSNs and for their application.

Former studies by several research groups have demonstrated that incorporation of copper successfully modifies optical, catalytic and magnetic properties of transition metal oxides. Hammad et al.[13] reported room temperature ferromagnetic (FM) ordering in zinc oxide (ZnO) nanoparticles were doped with up to 5 wt% Cu. They have also noted an expansion of the band gap from 3.33 eV to 3.55 eV. Tobaldi et al.[14] studied hybrid Cu-modified titanium dioxide (TiO_2) nanoparticles and reported that they were able to tune

their photochromic properties, which was a novel observation for this system. Mohanapandian et al.[15] investigated the effect of Cu doping in chromium oxide nanoparticles. However, they did not report any core shell formation or any information regarding the nanoparticles' magnetic properties.

My previous study has shown promising results for copper modified chromium oxide magnetic nanoparticles. It was found that when modified by incorporating 2.28 at% copper, α-Cr_2O_3@α-$Cu_{19}Cr_{1.81}O_{2.87}$ CSNs display a weak FM/FiM nature (H_C ~ 292 Oe at 5 K) and an exchange bias effect (H_{EB} ~161 Oe and M_{EB} ~0.0134 emu/gm at 40 K) which is reduced and eventually vanishes with increasing temperature increases until room temperature is reached. However, that study did not consider the optimization of Cu atom concentration for achieving desirable magnetic property, i.e., FM/FiM behavior at and above room temperature.

In the current study, I have synthesized Cu α-Cr_2O_3@α-$Cu_xCr_{2-x}O_3$ CSNs having copper concentrations in the 3.92 to 7.68 at% range. The structural characterization was performed using x-ray diffraction (XRD), x-ray photoelectron spectroscopy (XPS), transmission electron spectroscopy (TEM) and energy dispersive x-ray spectroscopy (EDX). For magnetic measurements, a vibrating sample magnetometry (VSM) was used.

Experimental

Synthesis of CSNs. For synthesis of CSNs, the first step was the preparation of α-Cr_2O_3 nano particles using a microwave assisted method described previously[10,16]. Afterwards, the hydrothermal nanophase epitaxy method developed in our lab was used to synthesize the shell region of the CSNs[10]. During the later process, the concentrations

of dopant salt solution containing dopant ions were varied to create the difference of copper percentage in the chromium oxide nanoparticles.

For the first step, commercially available triethanolamine (TEOA), $C_6H_{15}NO_3$ was used as a precursor. First, 11.67 gm of chromium (III) nitrate nonahydrate, $Cr(NO_3)_3.9H_2O$ was taken in 145.8 mL of DI water to prepare a 0.20 M aqueous solution. Separately, 26.85 gm of triethanolamine was taken in 450 mL of DI water. The two solutions were then mixed together and stirred for 30 minutes at a speed of 8 revolutions per minute. Subsequently, the solution was placed in a microwave oven and heated for 20 minutes. The 50 minutes cycle of stirring and heating was repeated five times. It was then placed on a hot plate and mild heating was continued until most of the water was evaporated and the solution turned into a dark green thick slurry. At this stage, the slurry was transferred in a ceramic boat and placed in a furnace at 750 °C in atmospheric oxygen environment for four hours. The residue left in the boat at the end of this solution consisted of α-Cr_2O_3 nanoparticles.

In the next step, the α-Cr_2O_3 nanoparticles were hydrothermally treated in a solution containing Cu^{2+} ions; the pH of the solution was maintained at ~ 3.6. We conjecture that the original nanoparticles undergo slight dissolution and at the same time host Cu^{2+} ions are incorporated in the re-precipitation of the Cu-chromia onto the surface of the nanoparticles, at high temperature and hydrostatic pressure conditions. For charge balance, there should be formation of oxygen vacancies in the shell of the CSNs.

The copper chloride (97%), $CuCl_2$ used for this study was bought from Aldrich Chemical Company, Inc. HPLC water of 18.2 MΩ resistance was used for solution preparation, which was deoxygenated using nitrogen purging while slightly heating on a

hot plate at around 80ºC temperature. First, 0.18 gm, 0.27 gm and 0.36 gm of $CuCl_2$ was added to 20 mL of water to obtain solutions having concentrations 0.10 M, 0.15 M and 0.20 M, respectively. Then each solution was added with 0.22 gm of chromium oxide nanoparticles and sonicated for 30 minutes. The model of the instrument used for sonication is Cole-Parmer 8890. The solutions were then separately placed in Teflon sleeves which were then inserted in hydrothermal reactor autoclaves and tightened properly. The autoclaves were then left inside a box type muffle furnace (using nichrome wire as the heating element) at 180 °Celsius for 24 hours. The cooling of the autoclave was made inside the furnace. The particles were then rinsed (using DI water) 5 times. The rinsing procedure included leaving the samples undisturbed for long hours so that the heavier nanoparticles precipitate/deposit at the bottom and lighter residue is collected near the top. Then the solution from the top portion was decanted. After repeating the rinsing process 5 times, the water-nanoparticle mixture was poured on glass plates and left to dry by evaporation. The dried residue was then harvested and transferred to a molybdenum boat. It was then calcined using a Linkam Stage at 450 °Celsius for 4 hours in forming gas (mixture of 95 vol% Argon and 5 vol% hydrogen) environment (at 2 mm Hg pressure). The product of calcination was dark green nanoparticles.

Transmission electron microscopy (TEM). A vital step for transmission electron microscopy is sample preparation. Finding an appropriate dispersion medium for magnetic nanoparticles is always challenging. For my previous study, I obtained best dispersion using hexane, C_6H_{14}. Therefore, I used reagent grade hexane manufactured by Carolina Biological Supply Company (CAS # 110-54-3) for preparing samples under this study. The specimens for TEM were produced by putting approximately 1mg of samples

in a 5 mL vial containing hexane and then sonicating the solution for 30 minutes. After this step, the solution turned pale green and became mildly warm; a lacy grid was dipped in the solution for 5 seconds and then dried in air for several minutes. The grids were then gently placed inside cleaned grid holders. The instrument used for this study was an FEI Titan 80-300 Transmission Electron Microscope. The operating voltage of the field emission gun was maintained at 300 keV. For low resolution, both bright field and dark field imaging were employed. However, all high-resolution images were taken in bright field. ImageJ software was used for data analysis. The scale was first adjusted and the lateral dimensions of at least 50 particles were measured and tabulated for each sample type. A Gaussian function was then fitted in the frequency versus size plot. The function provided the mean value of the distribution. The results of the TEM analyses are tabulated in Table 3.1. The low-resolution images and size distribution analysis of 6.17 at% Cu-Cr_2O_3 CSNs is shown in Figure 3.1.

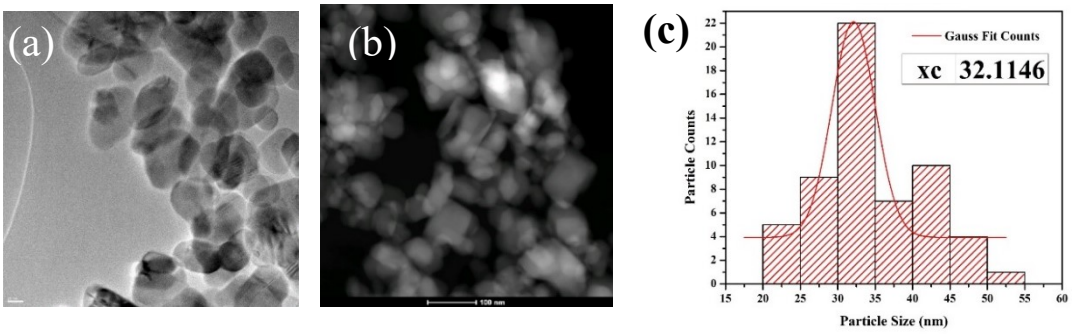

Figure 3.1: (a) and (b) Low resolution TEM images of 6.17 at% Cu-Cr_2O_3 CSNs; (c) the corresponding particle size distribution.

Figure 3.2(a) shows a high resolution TEM (HR-TEM) image of a single 6.17 at% Cu-Cr_2O_3 CSN. In Figure 3.2(b), a magnified region of the TEM image of the CSN shows the characteristic contrast between the core and shell regions.

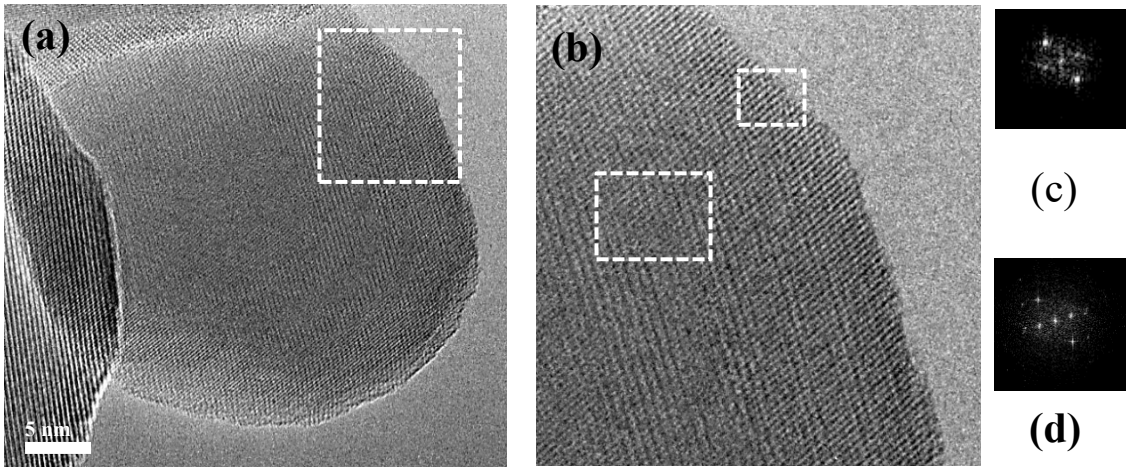

Figure 3.2: (a) HR-TEM image of a single 6.17 at% Cu- Cr_2O_3 CSN; (b) a magnified view of the core and shell region showing characteristic contrast; a fast Fourier transform (FFT) of (c) the shell region and (d) of the core region.

Table 3.1: Particle size obtained from XRD data and TEM images

	Particle Size from XRD (nm)	**Particle Size (nm)**	**Sigma (nm)**	**FWHM**
Pure	28.5	27.6	3.1	7.4
Sample 1	34.3	35.3	3.9	9.1
Sample 2	34.4	32.1	2.9	6.8
Sample 3	37.7	34.5	4.1	9.6

ImageJ was used for HR-TEM data analysis. Distinct core and shell regions were found to have formed in our CSNs, as indicated by the contrast differences and presence of defects in the interface regions in the HR-TEM images. Also, fast Fourier transforms (FFT) of both parts were taken, which produced the same pattern in reciprocal space. This shows that the core and shell of the CSN have the same corundum structure. The LR-TEM images and corresponding particle distribution and HR-TEM images for α-Cr_2O_3, 3.92 at% Cu-Cr_2O_3 and 7.68 at% Cu-Cr_2O_3 CSNs are shown in Appendix B.

X-Ray Photoelectron Spectroscopy (XPS). The model of the XPS instrument used for this study was a Thermo Scientific Alpha 110 hemispherical analyzer. The pass energy used in the instrument was 25 eV. The Kα irradiation of 1486.6 eV from aluminum was used as a monochromatic x-ray source. The $3d_{5/2}$ (binding energy 368.26 eV and full-width-half maxima, FWHM 0.36 eV) peak from silver (Ag) was used to perform calibration of the source and analyzer. The step size used for the high resolution XPS measurements was 0.1 eV, which was optimized for this sample. A flood gun was used to minimize charging effects. For analysis of the measured XPS data, CasaXPS 2.3.16 software package was used. The carbon 1s peak (284.8 eV) was used for calibration of the XPS data. The Shirley background function was used to model the background of the XPS. In select occasions, the peak centroid values were fixed, while the rest of the parameters were free to vary. For peak fitting, two different types of functions were used. The first one was a Gaussian-Lorentzian GL (30) function, which was used to fit more symmetrically shaped peaks. The second one was a Lorentzian functional form convoluted with Gaussian LA(a,b,n). This one was used to fit more asymmetrical peaks. Figure 3.3 shows the survey scan data of 6.17 at% Cu-Cr_2O_3. The XPS survey scan and high-resolution scan data for 3.92 at% Cu-Cr_2O_3 and 7.68 at% Cu-Cr_2O_3 are attached in Appendix B.

As evidenced from Figure 3.4, there is a significant charging contribution in several high-resolution peaks. To overcome this, an extra peak was used in the fitting to account for charging effects. The compositions obtained from analysis of HR-XPS data for three

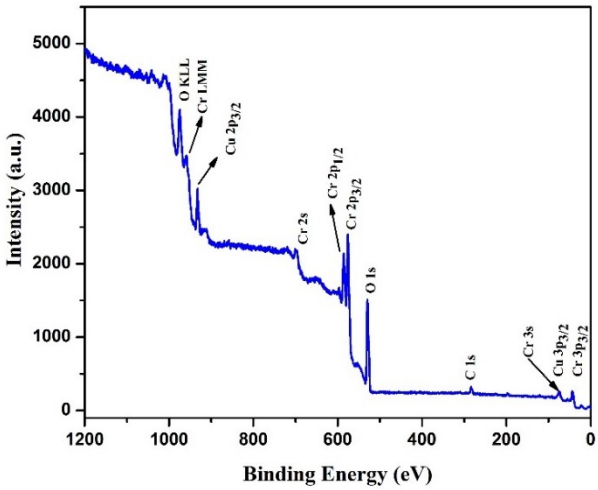

Figure 3.3: XPS Survey scan of 6.17 at% Cu- Cr_2O_3

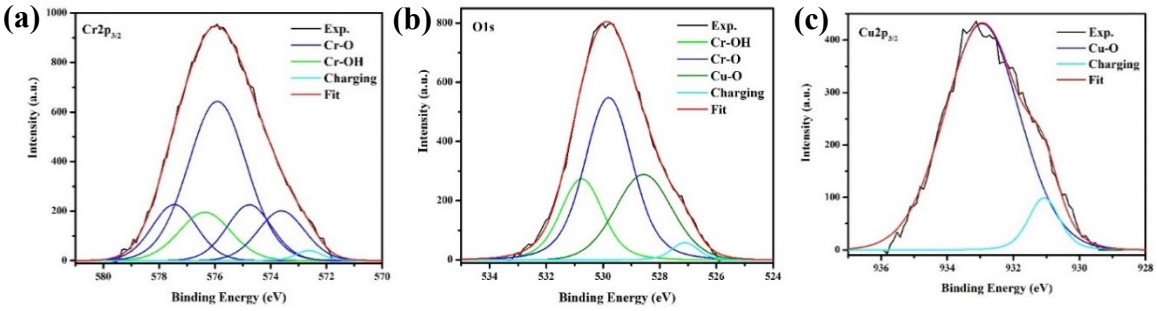

Figure 3.4: HR-XPS peak of (a) Cr $2p_{3/2}$ and (b) O1s and (c) $Cu2p_{3/2}$ of 6.17 at% Cu-Cr_2O_3

different particle species are summarized in Table 3.2. Particle diameter and shell thickness data were obtained from TEM image analysis.

Table 3.2: Chemical composition obtained from XPS analysis

Sample No.	Particle Diameter (nm)	Shell Thickness (nm)	At% Copper	At% Chromium	At% Oxygen	O/Cr
1	35.3	4.0	3.9	38.7	57.4	1.48
2	32.1	2.5	6.2	38.1	55.8	1.47
3	34.5	3.0	7.7	37.7	54.6	1.45

After obtaining the particle size and shell thickness (from TEM data), it is possible to use a model to determine the Cu concentration in the CSNs. First, the percentage of particle volume (z) of core and shell of a single nanoparticle from where the XPS signal gets collected (assuming a certain penetration depth, normally ~ 10 nm) is determined. Then, using the chemical concentrations obtained from XPS analysis, disregarding hydroxyl ions, a mathematical formula based on volume ratios and z allows for the determination of the Cu concentration in the shell of the CSNs. This method is shown for the calculation of CSNs containing 6.17 at% Cu in Appendix B. The results of these calculations are summarized in Table 3.3.

Table 3.3: Calculated shell formula of the CSNs

Sample No.	Cu Content	Molecular Formula
1	3.92 at%	α-Cr_2O_3@$Cu_{0.34}Cr_{1.66}O_{2.78}$
2	6.17 at%	α-Cr_2O_3@$Cu_{0.74}Cr_{1.26}O_{2.65}$
3	7.68 at%	α-Cr_2O_3@$Cu_{0.81}Cr_{1.19}O_{2.55}$

X-ray diffraction (XRD). For sample preparation for XRD, approximately 25 mg powder sample was poured on a clean glass slide. A few drops of ethanol was then mixed with the powder sample for better adhesion to the glass slide. The instrument used for x-ray diffraction study was a Bruker D8 diffractometer. The copper Kα irradiation of wave length λ=1.54184 Å was used as a monochromatic source. The voltage and current values used for the x-ray gun were 40 KV and 40 mA. All x-ray measurements were performed at room temperature. A Göbel mirror was used at incident beam/source side. Slits with 0.6 mm aperture were used on the source.

Bruker AXS GmbH TOPAS full pattern refinement program was used for data analysis[17], for two different objectives. Firstly, to extract particle size information and secondly, to perform structural analysis. For particles size measurement, the Scherrer formula constants k and s values were set to 0.9 and 0 respectively. The Lorentz Polarization (LP) factor was set to 27.3 and the FP peak type was selected.

For structural analysis, Symmetry Mode Rietveld refinement was performed. An LP factor value of 26.4 was used for this part. The fundamental parameter (FP) peak shape function was used. Zero error was refined. The isotropic Debye-Waller disorder factor (Beq) for both core and shell regions were constrained between 0.6 to 1.2. The scale factor was also refined. Two background functions, namely a Chebychev polynomial and 1/X functions were used to model the background of data[17]. The order of Chebychev polynomial used was 9. The Rietveld refinement was performed for both the pure α-Cr_2O_3 and α-Cr_2O_3@α-$Cu_xCr_{1-x}O_3$ CSNs starting with a corundum (Al_2O_3) structure (ICSD 173470) of space group R-3cH. The lattice parameters obtained from Rietveld refinement of pure α-Cr_2O_3 phase were used as initial input values in the refinement of the XRD measured from the α-Cr_2O_3@α-$Cu_xCr_{1-x}O_3$ CSNs. The particle size used in the refinement was set at the value obtained from TEM low resolution image analysis. To simulate the shell, the Cu^{2+} and Cr^{3+} ions with different partial occupancies were used for the cation sites.

The result of size analysis using Scherrer[18] formula are summarized in table 3.4. The fitted XRD data of Rietveld refinement for sample 2 (α-Cr_2O_3@α-$Cu_xCr_{1-x}O_3$) is presented in Figure 3.5. The fitted XRD data measured from samples 1 and 3 are given in

the Appendix B included at the end of this thesis. Two tables summarizing the parameters used for analysis of XRD using Topas are also included in the Appendix B.

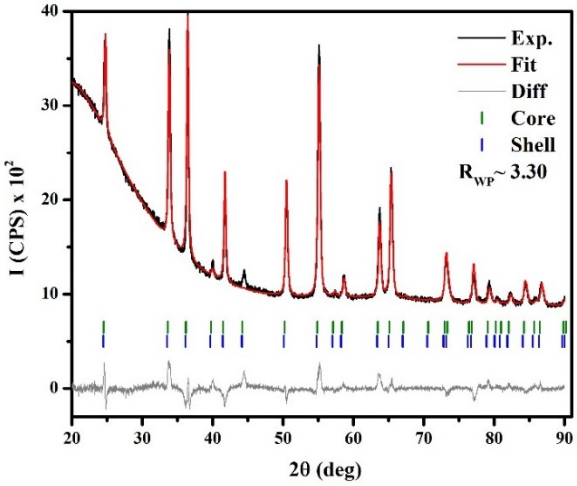

Figure 3.5: The Rietveld refinement of Cu 6.17 at% CSN (sample 2) XRD data. The vertical marks show the Bragg angle position for core (green) and shell (brown).

Table 3.4: Summary of structural information gathered through Rietveld refinement of XRD data of α-Cr_2O_3@$Cu_{0.74}Cr_{1.26}O_{2.65}$ CSNs.

Core: α-Cr_2O_3 NPs					
	a (Å)	b (Å)	c (Å)	Volume (Å^3)	Core Size (nm)
	4.958	4.958	13.584	289.186	28.65
Atoms	x	y	z	Occupancy	Beq. (Å^2)
Cr	0	0	0.35180	1.0	0.6
O	0.31940	0.08218	0.25000	1.0	1.2

Shell: α-Cr_2O_3@$Cu_{0.74}Cr_{1.26}O_{2.65}$					
	a (Å)	b (Å)	c (Å)	Volume (Å^3)	Shell Size (nm)
	4.9620	4.9620	13.614	290.288	25.465
Atoms	x	y	z	Occupancy	Beq. (Å^2)
Cr	0	0	0.30306	0.63	1.199
O	0.31940	0	0.25000	0.88	0.600
Cu	0	0	0	0.37	0.600

Magnetic measurements. The hysteresis measurements at 10 K for samples 1, 2 and 3 are shown in Figures 3.6(a), 3.6(c) and 3.6(e), respectively. The results of the M vs T measurements for samples 1, 2 and 3 are shown in Figures 3.6(b), 3.6(d) and 3.6(f), respectively.

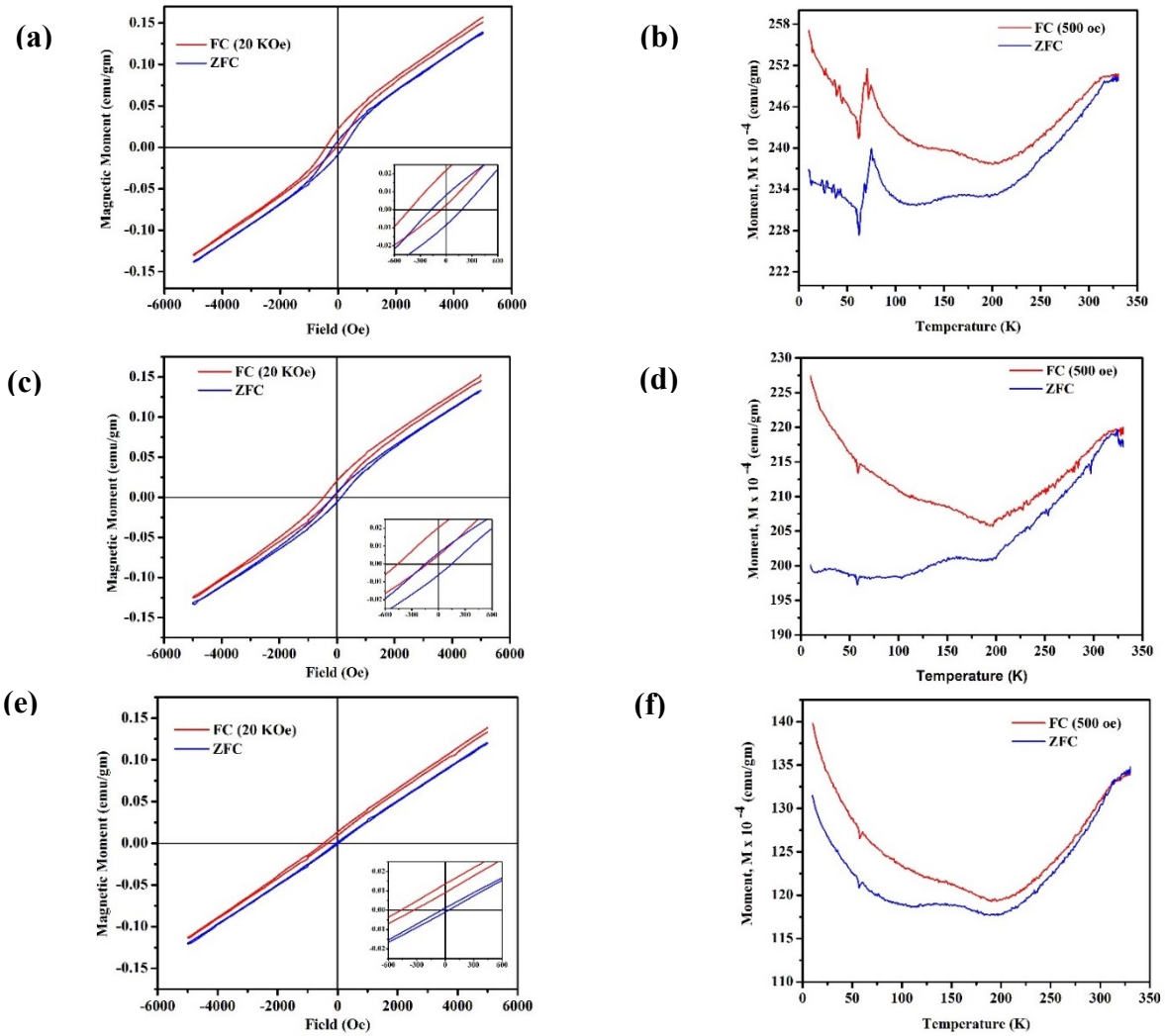

Figure 3.6: Field cooled (FC) and zero field cooled (ZFC) hysteresis loops of (a) 3.92 at% Cu-Cr_2O_3, (c) 6.17 at% Cu-Cr_2O_3, and (e) 7.68 at% Cu-Cr_2O_3 CSNs measured at 10 K; M Vs T plots of (b) 3.92 at% Cu-Cr_2O_3, (d) 6.17 at% Cu-Cr_2O_3, and (f) 7.68 at% Cu-Cr_2O_3 CSNs.

The instrument used for the magnetic measureerements was a Vibrating Sample Magnetometer (VSM). For all three samples, hysteresis (magnetic moment, M Vs field,

H) measurements were performed in both the field cooled (FC) and zero field cooled (ZFC) conditions at 10 K.

For field cooled hysteresis measurement, the sample was first centered and heated to 330 K (well above the Néel temperature of α-Cr_2O_3, causing it to convert to a paramagnetic state). Then a field of 20 kOe was applied while cooling the sample down to 10 K. At 10 K, a hysteresis measurement was performed between -5000 Oe and 5000 Oe field. After that, the sample was heated back to 330 K and cooled without applying any field for ZFC measurement and again a hysteresis loop was plotted between -5000 Oe and 5000 Oe field range. In addition, temperature dependent FC and ZFC hysteresis curves were measured for sample 2 at temperatures ranging from 10 to 300 K. Select measurements from this set of data are shown in Figure 3.7.

For M vs T measurement, the sample was first centered again and the temperature was raised to 330 K. A field of 500 Oe was then applied during cooling the sample down to 10 K. A stable magnetic field of 500 Oe was applied while collecting data for M vs T measurements. The M vs T were measured from 10 K to 330 K. For ZFC measurement, the sample was again heated up to 330 K and then cooled down to 10 K without an applied magnetic field. During data collection from 10 K to 330 K, a stable magnetic field of 500 Oe was applied.

The hysteresis loops for sample 2 were measured at temperatures 10K, 40K, 80K, 130K, 200K and 300K, in both FC and ZFC conditions. The field applied for FC measurement was same as quoted above (20 KOe). The results of these measurements are displayed in Figure 3.7. Origin 8.5 software was used to analyze the obtained data. Figure

3.8 shows the composition relative analysis of magnetic data and Figure 3.9 displays the temperature relative analysis of magnetic data of sample 2.

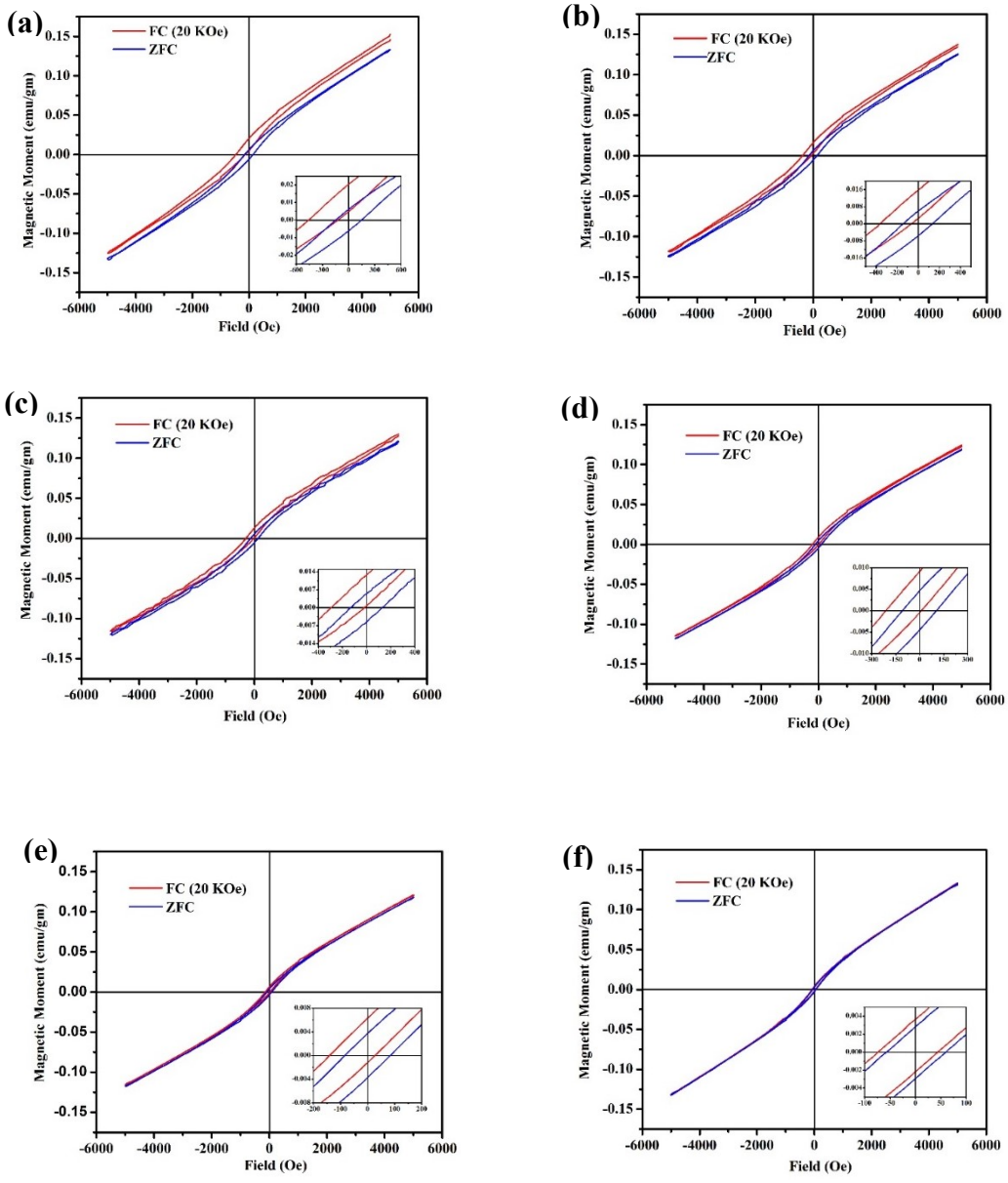

Figure 3.7: Field cooled (FC) and zero field cooled (ZFC) hysteresis loops of 6.17 at% Cu containing Cr_2O_3-based CSNs at (a) 10 K, (b) 40 K, (c) 80 K, (d) 130 K, (e) 200 K and (f) 300 K.

The formula used for coercivity measurement was $Hc=|(H_L-H_R)/2|$, where H_L and H_R are left and right zero field crossing points of the loops, respectively. Similarly, the

formula for remanence, $M_R=|(M_T-M_B)/2|$, where M_T and M_B are top and bottom zero magnetic moment crossing points of the loops, respectively. The value of horizontal exchange bias, H_{EB} was measured as the absolute value of the horizontal shift (in H axis) of the center of the FC hysteresis loop relative to the un-shifted ZFC loop. Similarly, the

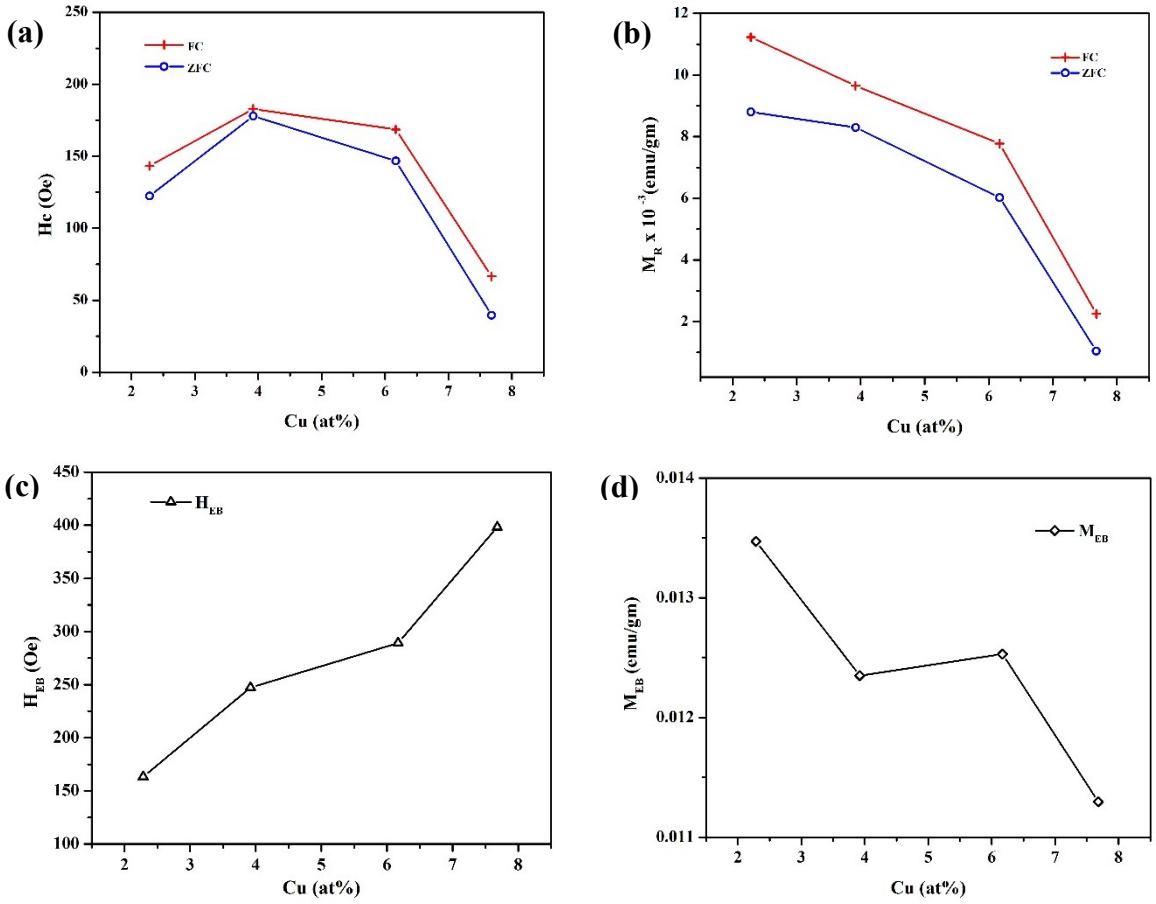

Figure 3.8: (a) Coercivity (H_C) versus at% of Cu, (b) remanence (M_R) versus at% of Cu, (c) horizontal exchange bias, H_{EB} versus at% of Cu, (d) vertical exchange bias, M_{EB} versus at% of Cu.

value of the vertical exchange bias, M_{EB} was measured as the absolute value of the vertical shift (in M axis) of the center of FC hysteresis relative to the ZFC loop.

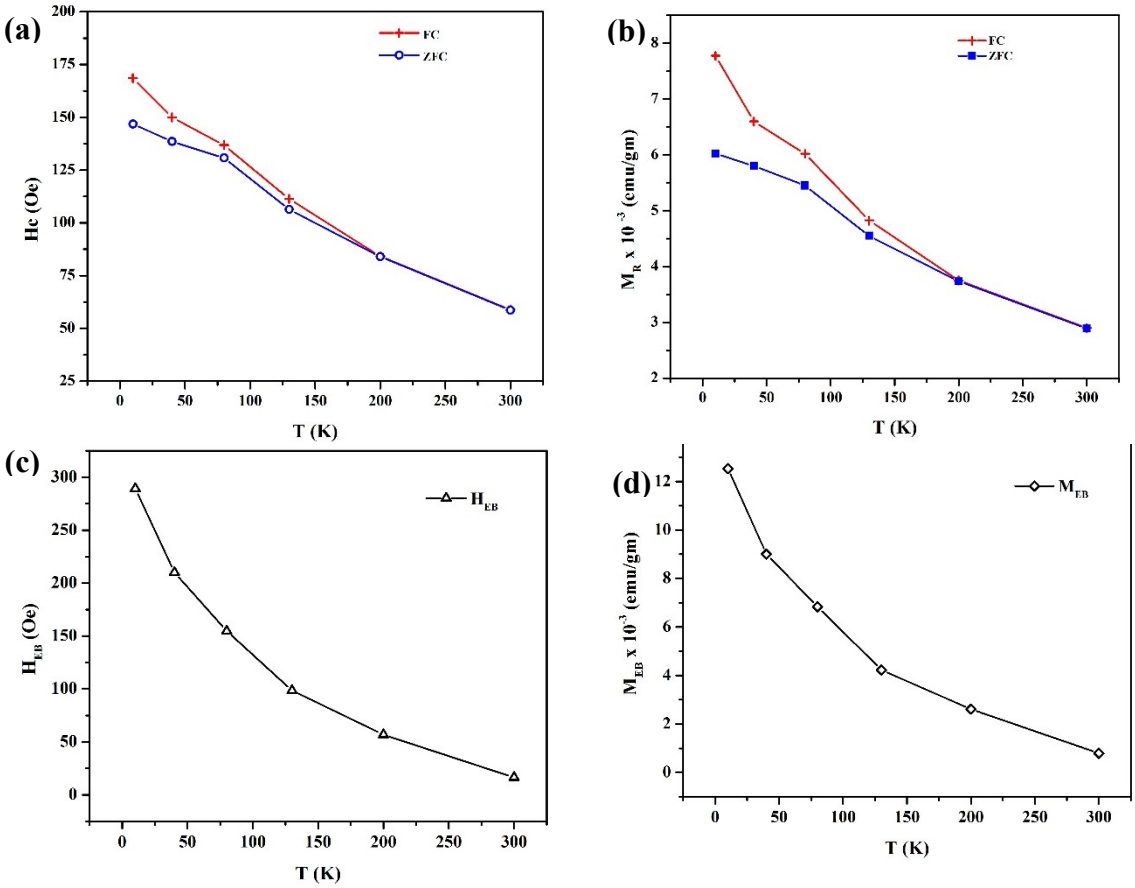

Figure 3.9: (a) Coercivity, H_C versus T, (b) remanence, M_R versus T, (c) horizontal exchange bias, H_{EB} versus T, and (d) vertical exchange bias, M_{EB} versus T for sample 2 CSNs.

Results and Discussion

The low resolution TEM images (Figures 3.1(a) &3.1(b), 3.2(a), (b) and 3.3 (a), (b)) reveal the overall particle shape to be pseudo spherical and faceted for all three samples. The full width half maxima (FWHM) and sigma (σ) values suggest that sample 2 has the narrowest distribution. The particle size obtained from XRD data using Scherer formula was within (±10%) to that values obtained from the TEM images.

The XRD data show that the corundum structure is maintained throughout the core and shell. Since Cu^{2+} is larger in diameter than Cr^{2+}, it is expected that the shell region will have a slightly larger average lattice parameter. In the XRD data, this should

be evident by a shift of the peaks to lower angle values. The results of the Reitveld refinement for sample 2 are summarized in Figure 2.5. Two different phases were used for peak fitting, one of which is pure corundum structure (α-Cr_2O_3) for the core; the other is a modified corundum structure (labelled as shell). Instead of single cation species, two different cation species (Cr^{3+} & Cu^{2+}) are included in the shell structural phase. The occupancy values of the ions were set according to the calculated shell composition using a combination of TEM and XPS results. The Rietveld refinement results indicate that the nanoparticles have a core-shell structure. Figures 3.2(a) and 2.2(b) shows HR-TEM images of sample 2. The fast Fourier transforms (FFT) of the core (Figure 3.2(c)) and shell (Figure 3.2(d)) regions show that the corundum structure is maintained throughout core and shell. Similar conclusions could be reached by analyzing HR-TEM images of sample 1 (Figure (3.14(a) and 3.14(b)) and sample 2 (Figure 3.15(a), 3.15(b)) attached in the supplementary information section. To determine the Cu content of the CSNs, the analysis of the XPS survey spectra shows that 3.92 at% Cu, 6.17 at% Cu and 7.68 at% Cu are present in samples 1,2 and 3, respectively. Detailed analyses of the Cr $2p_{3/2}$ XPS peak reveals that there are two different types of Cr binding: one of which is bonded with oxygen (Cr-O) and another is bonded with the hydroxyl ion (Cr-OH). The analysis of the Cu $2p_{3/2}$ peak shows that Cu is in the 2+ oxidation state. The O 1s peak shows presence of hydroxyl ion (OH^-) and O bonded with Cr (e.g., Cr-O) and Cu (e.g., Cu-O). Charging effects, as observed in the form of a small shoulder in the lower energy side of the XPS peaks, were accounted for by inclusion of an additional peak in the fitting.

Results for the H_{EB} and Hc values determined from the magnetic hysteresis measurements are shown in Figures 3.8 and 3.9. Here, I have included data from Cu-

chromia based CSNs obtained in my first study (Chapter 1). Note that the hysteresis data for the 2.28 Cu at% CSN sample were measured at 5 K whereas the hysteresis data for samples 1 to 3 were measured at 10 K. The comparison is valid because H_{EB}, H_C and M_R values are expected to be only slightly reduced at 10 K for the 2.28 Cu at% CSN sample. These data clearly show that overall, H_C is maximal for 3.92 at% Cu concentration in the CSNs. This behavior can be attributed to a concentration dispersion effect. As the concentration of Cu^{2+} ion increases, their greater proximity leads to an increase in the FM/FiM interactions in the shell of the CSNs. However, after reaching a maximum dispersal vs concentration, the FM/FiM interactions decrease due to a saturation effect whereby the proximity of the Cu^{2+} ions to each other becomes too great effectively quenching the FM/FiM interactions. The implication of our results is that it is the Cu-O-Cr interactions that appear to be most important in giving rise to the FM/FiM properties to our CSNs.

I observe that a kink appears in both the FC and ZFC M vs T data starting at ~ 60 K for all of the CSNs of this study (including for the Cu-chromia CSNs of my previous study shown in Chapter 1). I speculate that this is due to a freezing transition of spins that have the characteristics of a spin glass. The spins initially freeze in a spin glass like state during cooling to a rather low temperature. Furthermore, the spins remain frozen until they reach a temperature (just below the freezing temperature) where the spins are provided sufficient energy to move. However, at this juncture, the spins are not capable of arranging in a completely random fashion with respect to one another (i.e., this is not a so-called canonical spin glass). Thus, the magnetization rises for a short range with temperature. Then, after crossing a threshold which is closely related with the freezing

temperature, the excess thermal energy obtained from increased temperature adds to the randomness of the spin orientations of the system and the magnetization falls again back to the nominal level.

Note that the maximum inflection in the M vs T curve, in the vicinity of the freezing temperature, occurs for the 3.92 at% Cu-Cr_2O_3 CSNs, coinciding with the optimal Cu concentration for the coercivity and exchange bias effects. Thus, a conjecture is posed that the dispersion effect of the substitutional Cu^{2+} ion on the cation sublattice may also be responsible for the freezing spin transition observed in the M vs T data measured from the CSNS. However, more experiments are required to test this conjecture.

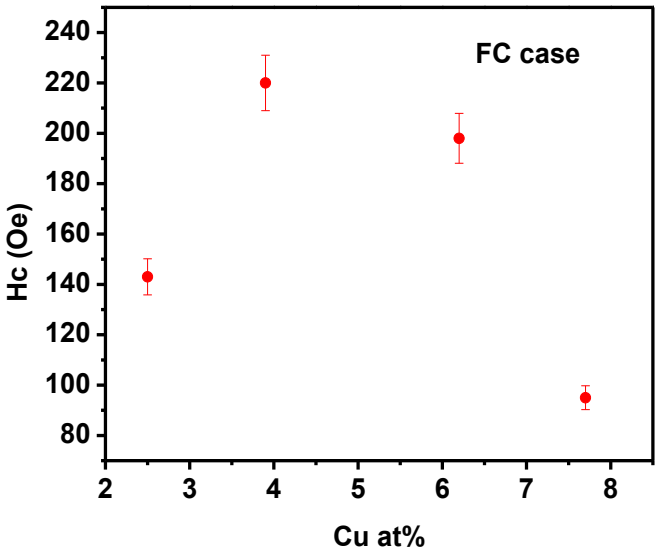

Figure 3.10: Variation in coercivity depending on copper percentage for FC measurement.

As shown in Figure 3.9, the coercivity and remanence measured from sample 2 in the FC case follow a decaying exponential dependence with increasing temperature. Figure 3.10 summarizes the observed concentration dependence of coercivity values.

Similar temperature dependence is also observed for the horizontal and vertical exchange bias field values for sample 2 (Figures 3.9(c) and (d)). A decaying exponential type temperature-dependence of the exchange bias is typical of the de-pinning of the uncompensated spins at the core-shell interface between AFM and FM/FiM regions. In the case of the Cu-chromia CSNs, the horizontal and vertical exchange bias mirror the coercivity and remanence in temperature dependence.

Conclusions

The HR-TEM images clearly show the formation of core-shell structure in the CSNs, the composition of which was obtained from HR-XPS data. The results of the magnetic measurements show that the magnetic properties, namely the introduction of the FM/FiM component and spin glass like behavior, of the CSNs are dependent on copper concentration. Furthermore, the FM/FiM properties are found to be most pronounced in the CSNs containing 3.92 at% Cu. These results demonstrate that the magnetic properties of α-Cr_2O_3@α-$Cu_xCr_{2-x}O_{3-y}$ are tunable by varying the copper concentration. I obtained (at 10 K) H_{EB} values of 247.2 Oe, 289.2 Oe and 398.2 Oe and M_{EB} values of 0.01235 emu/gm, 0.01253 emu/gm and 0.0113 emu/gm for CSN samples having Cu percentages of 3.92 at%, 6.17 at% and 7.68 at%, respectively. The Cr_2O_3–based CSNs having 6.17 at% Cu exhibit weak FM/FiM characteristics (coercivity~58.775 Oe and H_{EB} ~16.39 Oe) near room temperature (300K) conditions. The FM/FiM characteristics of the Cu-substituted chromia-based CSNs, coupled with the AFM core generates a temperature-dependent exchange bias effect. However, the reduction of the coercivity and exchange bias field at higher doping level may be attributed to dispersion coupled with a saturation

effect. A decaying exponential temperature-dependence of the exchange bias was observed for the α-Cr_2O_3@α-$Cu_xCr_{2-x}O_{3-y}$ CSNs, that may be associated with the de-pinning of the uncompensated spins at the AFM-FM/FiM core-shell interface.

References

1. López-Ortega, A., Estrader, M., Salazar-Alvarez, G., Roca, A. G. & Nogués, J. Applications of exchange coupled bi-magnetic hard/soft and soft/hard magnetic core/shell nanoparticles. *Phys. Rep.* **553,** 1–32 (2015).

2. Street, M. *et al.* Increasing the Néel temperature of magnetoelectric chromia for voltage-controlled spintronics. *Appl. Phys. Lett.* **104,** 222402 (2014).

3. O'Dell, T. H. Measurements of the magneto-electric susceptibility of polycrystalline chromium oxide. *Philos. Mag.* **13,** 921–933 (1966).

4. Hou, X. & Choy, K.-L. Synthesis of Cr_2O_3-based nanocomposite coatings with incorporation of inorganic fullerene-like nanoparticles. *Thin Solid Films* **516,** 8620–8624 (2008).

5. Spitz, R., Revillon, A. & Guyot, A. Supported chromium oxide catalyst for olefin polymerization. XI. comparison between ethylene and propylene polymerization. *J. Macromol. Sci. Part - Chem.* **8,** 1129–1136 (1974).

6. Rao, T. V. M., Zahidi, E. M. & Sayari, A. Ethane dehydrogenation over pore-expanded mesoporous silica-supported chromium oxide: 2. Catalytic properties and nature of active sites. *J. Mol. Catal. Chem.* **301,** 159–165 (2009).

7. Rakesh, Ananda, S. & Gowda, N. M. M. Synthesis of chromium(III) oxide nanoparticles by electrochemical method and Mukia Maderaspatana Plant extract, characterization, $KMnO_4$ decomposition and antibacterial study. *Mod. Res. Catal.* **02,** 127–135 (2013).

8. Teixeira, V. *et al.* Spectrally selective composite coatings of Cr–Cr_2O_3 and Mo–Al_2O_3 for solar energy applications. *Thin Solid Films* **392,** 320–326 (2001).

9. He, X. *et al.* Robust isothermal electric control of exchange bias at room temperature. *Nat. Mater.* **9,** 579–585 (2010).

10. Dey, S., Hossain, M. D., Mayanovic, R. A., Wirth, R. & Gordon, R. A. Novel highly ordered core–shell nanoparticles. *J. Mater. Sci.* **52,** 2066–2076 (2017).

11. Hossain, M. D., Dey, S., Mayanovic, R. A. & Benamara, M. Structural and magnetic properties of well-ordered inverted core-shell α-Cr_2O_3/ α-$M_xCr_{2-x}O_3$ (M=Co, Ni, Mn, Fe) nanoparticles. *MRS Adv.* **1,** 2387–2392 (2016).

12. Hossain, M. D., Mayanovic, R. A., Sakidja, R. & Benamara, M. An experimental and theoretical study of the optical, electronic, and magnetic properties of novel inverted α-Cr_2O_3@α-$Mn_{0.35}Cr_{1.65}O_{2.94}$ core shell nanoparticles. *J. Mater. Res.* **32,** 269–278 (2017).
13. Hammad, T. M., Salem, J. K., Harrison, R. G., Hempelmann, R. & Hejazy, N. K. Optical and magnetic properties of Cu-doped ZnO nanoparticles. *J. Mater. Sci. Mater. Electron.* **24,** 2846–2852 (2013).

14. Tobaldi, D. M. *et al.* Cu–TiO_2 hybrid nanoparticles exhibiting tunable photochromic behavior. *J. Phys. Chem. C* **119,** 23658–23668 (2015).

15. K. Mohanapandian & A. Krishnan. Synthesis, structural, morphological and optical properties of Cu^{2+} doped Cr_2O_3 nanoparticles. *Int. J. Adv. Eng. Technol.* **7,** 273–279 (2016).

16. Farzaneh, F. Synthesis and characterization of Cr_2O_3 nanoparticles with triethanolamine in water under microwave irradiation. *J. Sci. Islam. Repub. Iran* **22,** 329–333 (2011).

17. (2009)TOPASV4:General profile and structure analysis software for powder diffraction data. User's Manual. Bruker AXS,Karlsruhe,Germany.

18. Patterson, A. L. The Scherrer formula for X-ray particle size determination. *Phys. Rev.* **56,** 978–982 (1939).

CHAPTER 4: SUMMARY

In the first part of my thesis project, I studied copper- and, separately, aluminum-incorporated chromium oxide (chromia) CSNs. The size of the Cu-Cr_2O_3 and Al-Cr_2O_3 CSNs was determined from XRD and TEM analyses to be ~37 and 38 nm, with an average shell thickness of ~4 and ~5m, respectively. Analysis of high resolution XPS data gave concentrations of 2.28 at% Cu and 10.7at% Al in Cu-Cr_2O_3 and Al-Cr_2O_3 CSNs, respectively. The combined XRD and HR-TEM analysis provided evidence for the formation of core shell nanostructure and confirmed epitaxial growth of the shell over the core of the CSNs. The magnetic measurements using the SQUID showed that Cu-Cr_2O_3 CSNs are weakly FM/FiM at 5K whereas the Al-Cr_2O_3 CSNs showed predominantly AFM behavior at the same temperature. When compared to the hysteresis data of pure chromia, Al-Cr_2O_3 CSNs showed an increase in exchange bias value from 346.3 Oe (α- Cr_2O_3) to 462.6 Oe at 5 K.

In the second part of my thesis project, I performed a systematic study of the copper concentration dependency of magnetic characteristics of my modified chromia-based CSNs. Upon increase in Cu-incorporation (beyond 2.28 at% in the first part of the study) the HR-TEM images, provided strong evidence of core shell structure formation with presence of defects and misfit dislocations in the interface/shell region of the CSNs. The magnetic measurements revealed that upon increasing Cu concentration from 2.28 at% to 3.92 at% in the chromia-based CSNs results in an increase in coercivity value from 142.2 Oe to 182.56 Oe, accompanied by an increase in exchange bias (horizontal) value from 163.179 Oe to 247.22 Oe, at 5-10 K. Upon increasing the Cu concentration to

6.17 at% in the Cu-Cr_2O_3 CSNs, the coercivity dropped to 168.56 Oe while exchange bias value increased to 289.225 Oe at 10 K. Thus, in terms of the magnetic strength based on coercivity measure due to FM/FiM characteristics, it is predicted that the optimum level of Cu concentration is roughly in the 4-5 at% in Cu-Cr_2O_3 CSNs. The temperature dependent magnetic characterization of 6.17at% Cu modified chromia showed retention of FM/FiM characteristics starting from 10K until room temperature (coercivity 58.78 Oe and horizontal exchange bias 16.39 Oe in FC measurement at 300K). Therefore, it can be claimed that, obtaining room temperature FM/FiM behavior is possible by tuning the doping concentration in Cu modified chromia core shell nanoparticles system. A study on the effects of pressure during the hydrothermal process utilized in the HNE synthesis of Cu-Cr_2O_3 CSNs may reveal additional interesting nanostructure and magnetic properties of this system and may improve the tunability of the nanoparticles.

References

1. López-Ortega, A., Estrader, M., Salazar-Alvarez, G., Roca, A. G. & Nogués, J. Applications of exchange coupled bi-magnetic hard/soft and soft/hard magnetic core/shell nanoparticles. *Phys. Rep.* **553,** 1–32 (2015).

2. Nogués, J., Skumryev, V., Sort, J., Stoyanov, S. & Givord, D. Shell-Driven Magnetic Stability in Core-Shell Nanoparticles. *Phys. Rev. Lett.* **97,** (2006).

3. Meiklejohn, W. H. & Bean, C. P. New Magnetic Anisotropy. *Phys. Rev.* **102,** 1413–1414 (1956).

4. Street, M. *et al.* Increasing the Néel temperature of magnetoelectric chromia for voltage-controlled spintronics. *Appl. Phys. Lett.* **104,** 222402 (2014).

5. Li, P. *et al.* The effects of Al and Ba on the colour performance of chromic oxide green pigment. *Dyes Pigments* **80,** 287–291 (2009).

6. Carta, G. *et al.* A Comparative Study of Cr2O3 Thin Films Obtained by MOCVD using Three Different Precursors. *Chem. Vap. Depos.* **11,** 375–380 (2005).

7. Hou, X. & Choy, K.-L. Synthesis of Cr2O3-based nanocomposite coatings with incorporation of inorganic fullerene-like nanoparticles. *Thin Solid Films* **516,** 8620–8624 (2008).

8. Spitz, R., Revillon, A. & Guyot, A. Supported Chromium Oxide Catalyst for Olefin Polymerization. XI. Comparison between Ethylene and Propylene Polymerization. *J. Macromol. Sci. Part - Chem.* **8,** 1129–1136 (1974).

9. Rao, T. V. M., Zahidi, E. M. & Sayari, A. Ethane dehydrogenation over pore-expanded mesoporous silica-supported chromium oxide: 2. Catalytic properties and nature of active sites. *J. Mol. Catal. Chem.* **301,** 159–165 (2009).

10. Teixeira, V. *et al.* Spectrally selective composite coatings of Cr–Cr2O3 and Mo–Al2O3 for solar energy applications. *Thin Solid Films* **392,** 320–326 (2001).

11. Rakesh, Ananda, S. & Gowda, N. M. M. Synthesis of Chromium(III) Oxide Nanoparticles by Electrochemical Method and Mukia Maderaspatana Plant Extract, Characterization, KMnO4 Decomposition and Antibacterial Study. *Mod. Res. Catal.* **02,** 127–135 (2013).

12. Woo, Y. T., Lai, D. Y. & Arcos, J. C. *Natural, Metal, Fiber, and Macromolecular Carcinogens: Structural Bases and Biological Mechanisms*. (Elsevier Science, 2013).

13. He, X. *et al.* Robust isothermal electric control of exchange bias at room temperature. *Nat. Mater.* **9,** 579–585 (2010).

14. Dey, S., Hossain, M. D., Mayanovic, R. A., Wirth, R. & Gordon, R. A. Novel highly ordered core–shell nanoparticles. *J. Mater. Sci.* **52,** 2066–2076 (2017).

15. M.D. Hossain, R.A. Mayanovic, R. Sakidja, M. Benamara & R. Wirth. Novel Fe-Incorporated a-Cr2O3 Core-Shell Nanoparticles with Stable Magnetic Moments at Room Temperature (Submitted). *Nano Lett.*

APPENDIX A

Transmission electron micrograph (TEM) of α-Cr_2O_3

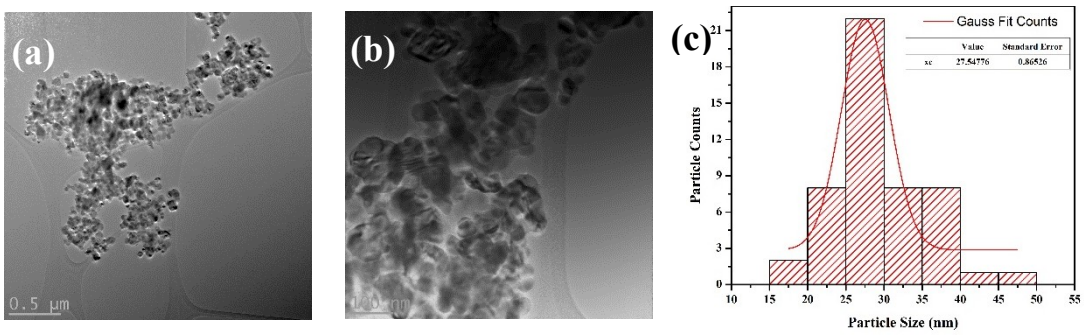

A.1: (a) and (b) Low resolution TEM images of pure Cr_2O_3, (c) corresponding particle distribution.

Example of Shell Formula Calculation for Cu-modified chromia nanoparticles

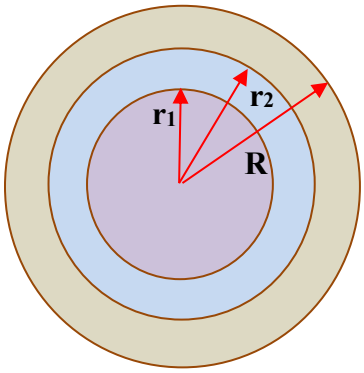

A.2: Model of a core-shell nanoparticle

First, we need to know what percentage of the XPS signal is coming from shell. For that, the following calculation was carried out using the model in Figure S1.2.

From analysis of TEM image, the average particle diameter, D = 36.5 nm

Therefore, the radius, R=18.25 nm

Overall core radius, r_2 = 14.25 nm (4 nm shell)

Radius of the core from where no x-ray signal is obtained, r_1 = 8.25 nm (assuming a 10 nm sampling depth)

So, the radius of core from where x-ray is collected should be r_2-r_1

Now, if z be the fraction of shell volume in total sampling volume then z can be written as,

z = (vol. of shell)/(sampling vol.)

$= (R^3-r_2^3)/(R^3-r_1^3)$

= 0.58 using dimensions above

Now the composition obtained from HR-XPS data analysis,

Cu:Cr:(O+OH) = 1.9: 32.63 : 65.47

However, if we ignore the portion oxygen which is bonded with hydrogen and renormalize the atomic percentages, the calculation yields,

Cu:Cr:O =2.28: 39.23 : 58.49

Calculation for x in shell:

Using, concentration in sampling vol. = $(1-z)\bullet[Cr_2O_3] + z\bullet[Cu_xCr_{(2-x)}O_p]$

We can write,

$0.0228Cu + 0.3922Cr + 0.5849O = 0.42\bullet[0.4Cr + 0.6O] + 0.58\bullet[yCu + (0.4261-y)Cr + 0.5739O]$

or, $0.0228Cu + 0.3922Cr + 0.5849O = 0.1691Cr + 0.2536O + 0.58yCu + 0.2460Cr - 0.58yCr + 0.3313O$

or, $0.0228Cu + 0.3922Cr + 0.5849O \approx 0.4151Cr + 0.5849O + 0.58y(Cu – Cr)$

or, $0.0228Cu - 0.0228Cr = 0.58y(Cu – Cr)$;

or, $0.0228 \approx 0.58y$

Therefore, $y = 0.0396$ which leads to $x = 5*0.0396 \approx 0.1979$

For oxygen vacancies: $0.5849[O] + O_{vacancy}\ [O_v] = 0.6[O]$ and $[O_v] = 0.0151$;

Thus, then $p = 3 – (0.0151*5)/0.6 = 2.87$.

Considering the XRD results, our best estimate of the (sub)stoichiometric formula of the shell is as follows:

Formula = $Cu_{0.19}Cr_{1.80}O_{2.87}$

APPENDIX B

TEM of Pure Cr_2O_3, Sample 1 and Sample 3

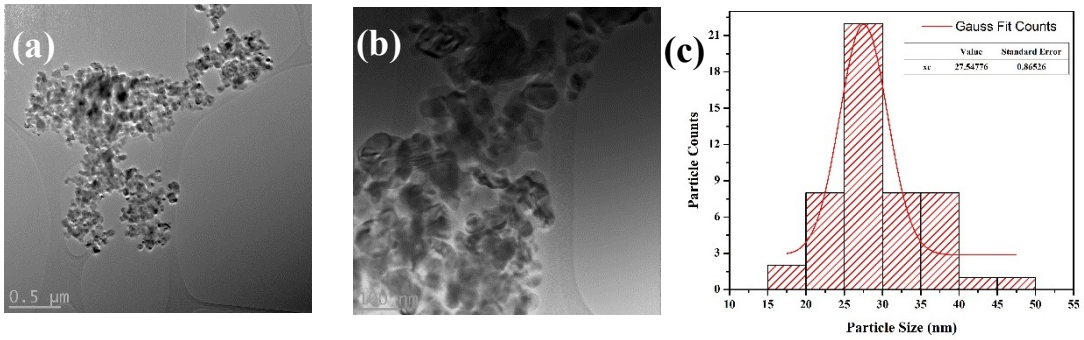

B.1: (a) and (b) Low resolution TEM images of pure Cr_2O_3; (c) the particle size distribution determined from images in (a) and (b).

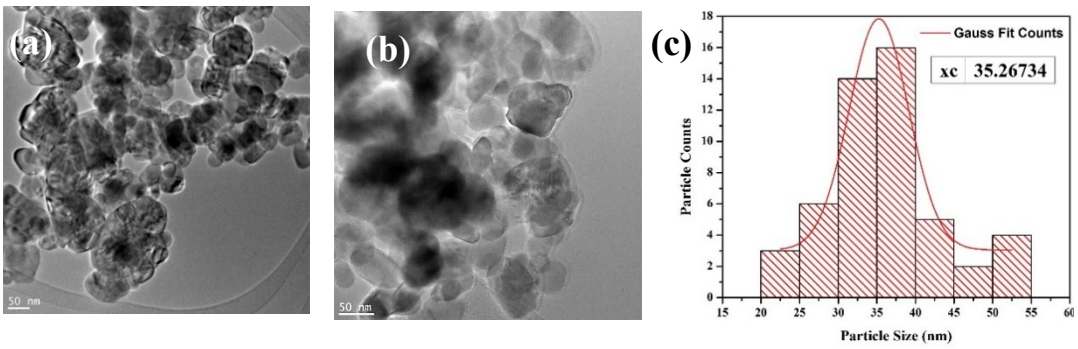

B.2: (a) and (b) Low resolution TEM images of sample having 3.92 at% Cu-Cr_2O_3 ; (c) the particle size distribution determined from images in (a) and (b).

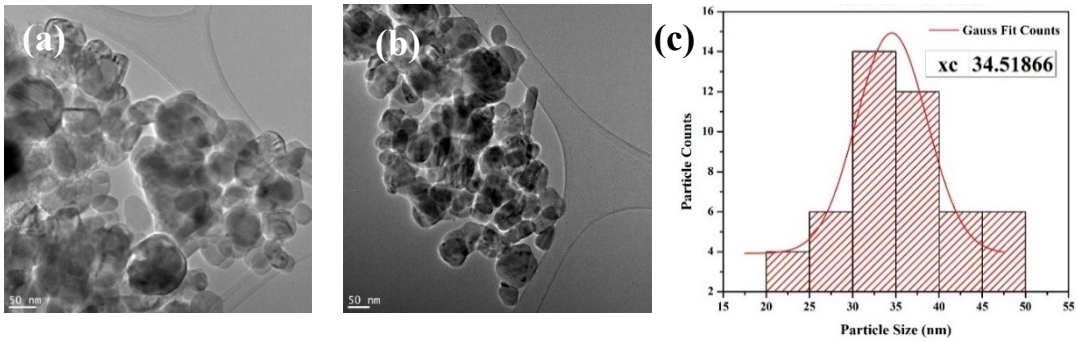

B.3: (a) and (b) Low resolution TEM images of CSN sample having 7.68 at% Cu- Cr_2O_3 ; (c) the particle size distribution determined from images in (a) and (b).

X-ray diffraction (XRD)

(a) **(b)**

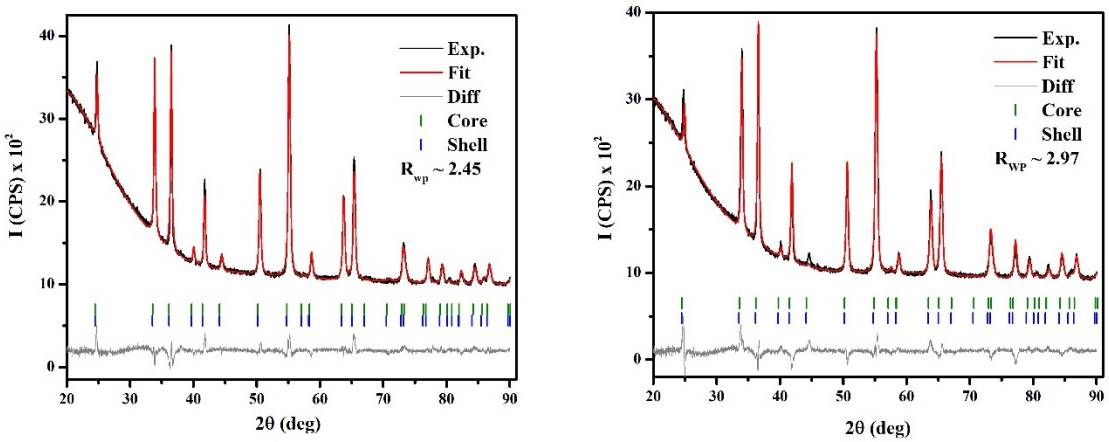

B.4: (a) The Rietveld refinement result of XRD data of (a) 3.92 at% Cu- Cr_2O_3 and (b) 7.68 at% Cu- Cr_2O_3 CSNs.

B.5: Summary of structural information gathered through Rietveld refinement of XRD data of 3.92 at% Cu- Cr_2O_3 core-shell nano-particles

Core: α-Cr_2O_3 NPs					
	a (Å)	b (Å)	c (Å)	Volume (Å^3)	Core Size (nm)
	4.958	4.958	13.59	289.3098	26.738
Atoms	x	y	z	Occupancy	Beq. (Å^2)
Cr	0	0	0.3518	1.0	0.6
O	0.31940	0	0.25	1.0	0.6

Shell: α-Cr_2O_3@$Cu_{0.34}Cr_{1.66}O_{2.78}$					
	a (Å)	b (Å)	c (Å)	Volume (Å^3)	Shell Size (nm)
	4.9612	4.9612	13.606	290.02	20.054
Atoms	x	y	z	Occupancy	Beq. (Å^2)
Cr	0	0	0.34145	0.81	0.600
O	0.29035	0	0.25	0.93	0.600
Cu	0	0	0.34062	0.19	0.600

B.6: Summary of structural information gathered through Rietveld refinement of XRD data of 7.68 at% Cu- Cr_2O_3 core-shell nano-particles.

Core: α-Cr_2O_3 NPs					
	a (Å)	b (Å)	c (Å)	Volume ($Å^3$)	Core Size (nm)
	4.959	4.959	13.59	289.368	28.648
Atoms	x	y	z	Occupancy	Beq. ($Å^2$)
Cr	0	0	0.3518	1.0	0.6
O	0.3194	0.0820	0.2500	1.0	1.2

Shell: α-Cr_2O_3@$Cu_{0.81}Cr_{1.19}O_{2.55}$					
	a (Å)	b (Å)	c (Å)	Volume ($Å^3$)	Shell Size (nm)
	4.965	4.965	13.615	290.669	31.83
Atoms	x	y	z	Occupancy	Beq. ($Å^2$)
Cr	0	0	0.3045	0.59	1.999
O	0.3100	0	0.2500	0.85	0.600
Cu	0	0	0.0000	0.41	0.600

HR-TEM Images of Cr_2O_3 –based CSNs having 3.92 at% Cu and 7.68 at% Cu

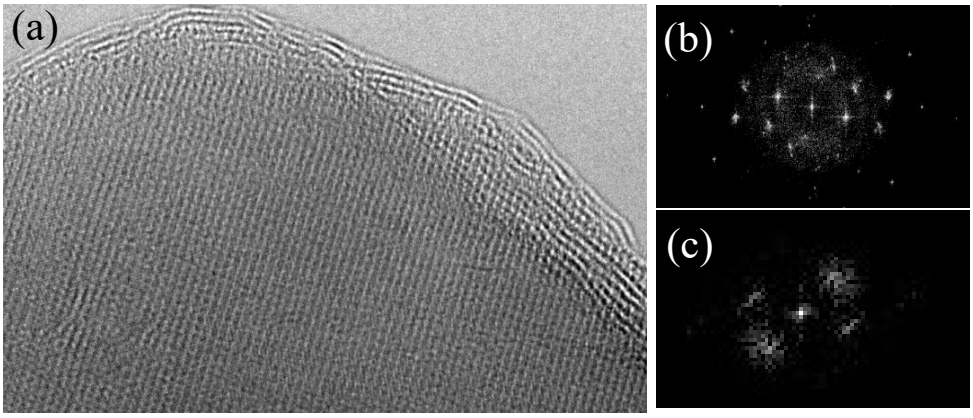

B.7: HR-TEM image of 3.92 at% Cu- Cr_2O_3 (a) magnified view of the core and shell region showing characteristic contrast and dislocations, (b) fast Fourier transforms (FFT) of core region and (c) of the shell region.

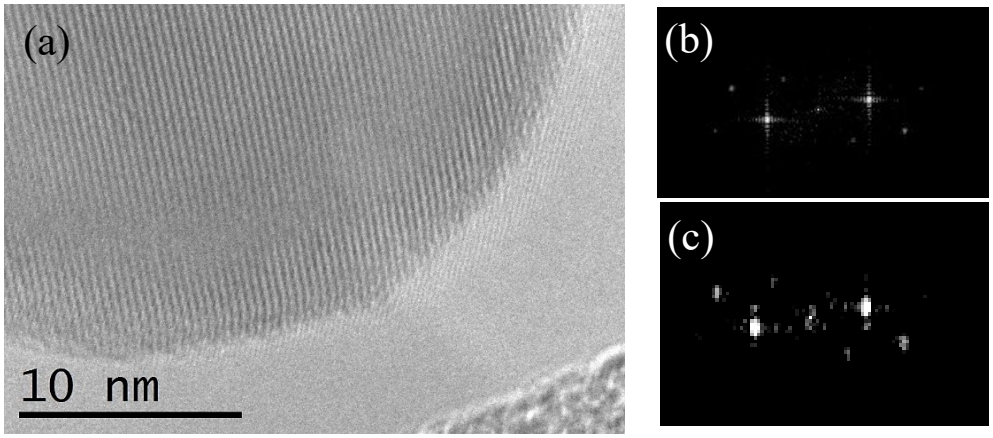

B.8: HR-TEM image of 7.68 at% Cu- Cr_2O_3 (a) magnified view of the core and shell region showing characteristic contrast and dislocations, (b) fast Fourier transforms (FFT) of core region and (c) of the shell region.

HR-XPS of 3.92 at% Cu-Cr_2O_3

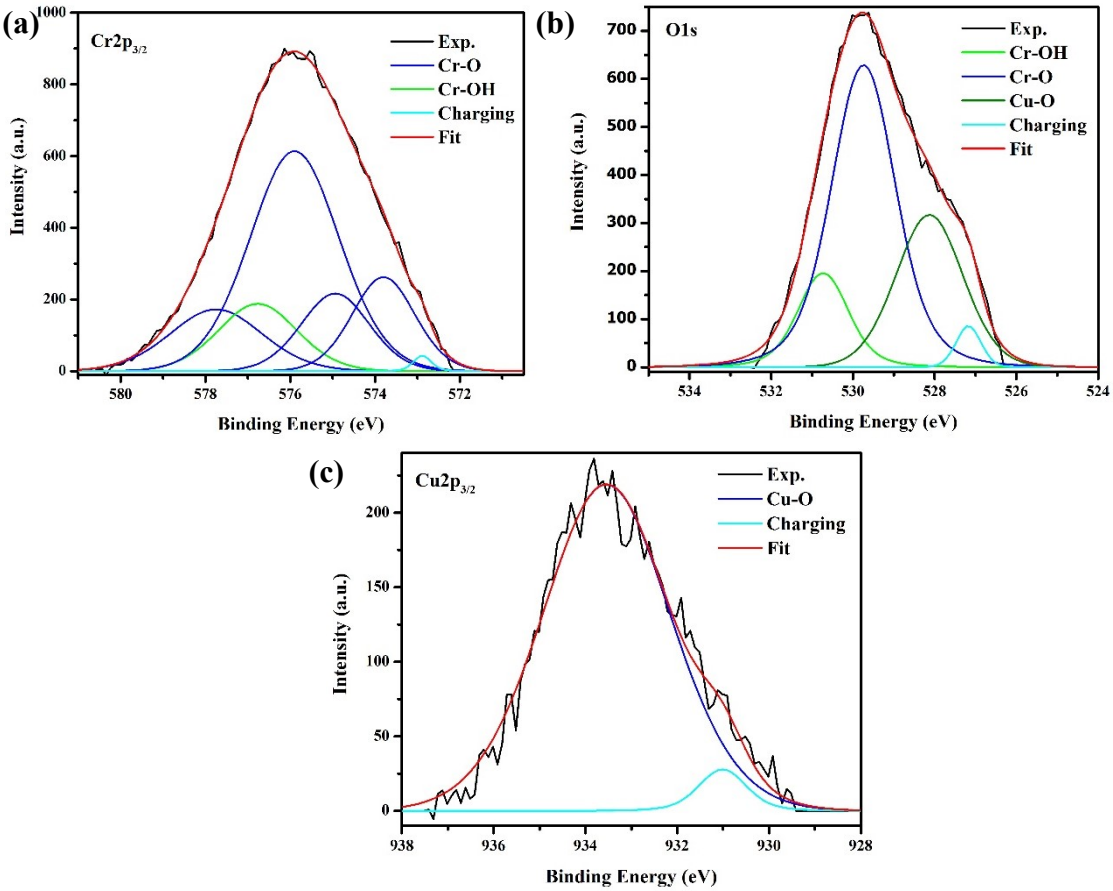

B.9: The (a) $Cr2p_{3/2}$ and (b) O1s and (c) $Cu2p_{3/2}$ HR-XPS peaks of 3.92 at% Cu- Cr_2O_3 CSNs.

HR-XPS of 7.68 at% Cu-Cr_2O_3

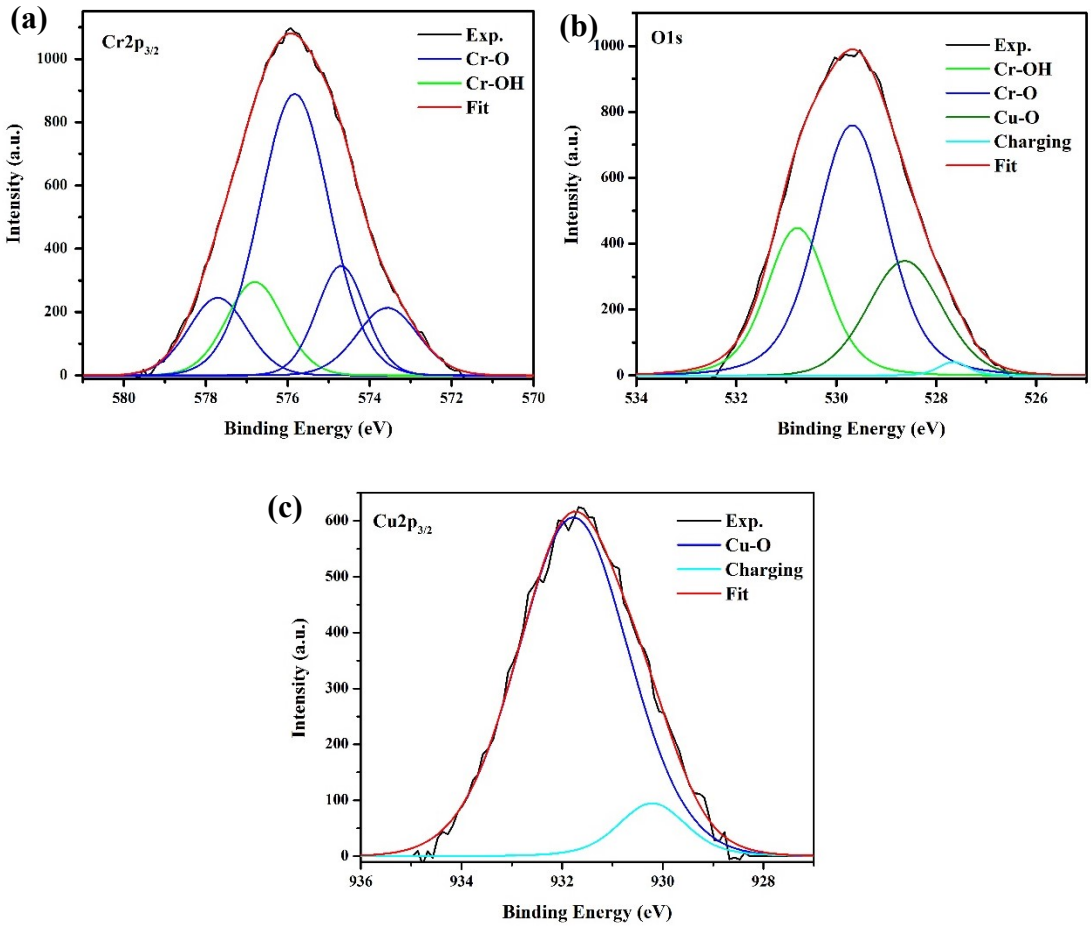

B.10: The (a) $Cr2p_{3/2}$ and (b) O1s and (c) $Cu2p_{3/2}$ HR-XPS peaks of 7.68 at% Cu- Cr_2O_3 CSNs.

Shell Formula Calculation of 7.68 at% Cu- Cr_2O_3

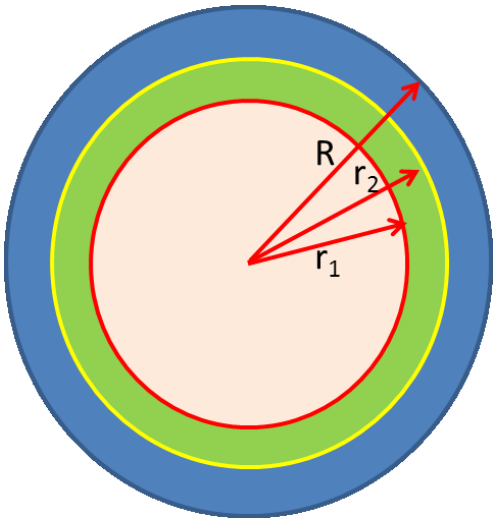

B.11: 2D model of CSNs

Here, the radius of nano-particle, R = 16.25 nm (D = 32.5 nm)

Radius of core, r_2 = 13.75 nm (2.5 nm shell)

Radius of core when no x-ray has reached, r_1 = 6.25 nm (10 nm sampling depth)

Let's, z be the fraction of shell volume in the overall signal/ data collection volume

Therefore, z = (vol. of shell)/(sampling vol.)

$= (R^3-r_2^3)/(R^3-r_1^3)$

= 0.42 (using dimensions above)

Now analysis of HR XPS data provide with the following at% values:

Cu:Cr:(O+OH) = 5.35: 32.98 : 61.68

Discarding the contribution from OH-, and renormalizing, we get

Cu:Cr:O =6.17: 38.05 : 55.79

Let's, x be the occupancy of copper or fraction of average chromium atoms substituted by copper in 1 molecule of Cr_2O_3 in shell region.

z be the fraction of shell molecules (modified by copper substitution) in overall sampling volume.

p be the average occupancy of oxygen in one shell molecule.

Using, concentration in sampling volume = $(1-z)\bullet[Cr_2O_3] + z\bullet[Cu_xCr_{(2-x)}O_p]$

We can write,

$0.0617Cu + 0.3805Cr + 0.5579O = 0.58\bullet[0.4Cr + 0.6O] + 0.42\bullet[yCu + (0.5008-y)Cr + 0.4992O]$

Or, $0.0617Cu + 0.3805Cr + 0.5579O= 0.232Cr + 0.348O + 0.42yCu+ 0.2104Cr - 0.42yCr + 0.2097O$

Or, $0.0617Cu + 0.3805Cr + 0.5579O = 0.4424Cr + 0.5579O + 0.42y(Cu – Cr)$

Or, $0.0617Cu - 0.0617Cr = 0.42y(Cu – Cr)$; or,

Or, $0.0617 = 0.42y$

so that $y = 0.147$,

thus $x = 5x\ 0.147$

Or, $x = 0.735$

For oxygen vacancies: $0.5579[O] + Ovacancy\ [Ov] = 0.6[O]$ and $[Ov] = 0.0421$; thus if Op then

$p = 3 – (0.0421 \times 5)/0.6 = 2.65$.

Taking into account the XRD results, our best estimate of the (sub)stoichiometric formula of the shell is as follows:

Formula = $Cu_{0.73}Cr_{1.26}O_{2.65}$

B.12: Magnetic parameters for CSNs of this study

at% Cu	Coercivity, H_C (Oe)		Remanence, M_R (emu/gm)		H_{EB} (Oe)	M_{EB} (emu/gm)
	FC	ZFC	FC	ZFC		
2.28	143.2	122.4	0.0112	0.0088	163.2	0.0135
3.92	182.8	177.9	0.0097	0.0083	247.2	0.0124
6.17	168.6	146.8	0.0078	0.0060	289.2	0.0125
7.68	66.5	39.5	0.0023	0.0011	398.2	0.0113

B.13: Temperature-dependent magnetic parameters of sample 2

Temperature (K)	Coercivity (Oe)		Remanence (emu/gm)		H_{EB} (Oe)	M_{EB} (emu/gm)
K	FC	ZFC	FC	ZFC		
10	168.7	146.8	0.0078	0.0060	289.2	0.0125
40	150.0	138.6	0.0066	0.0058	210.0	0.0090
80	136.8	130.8	0.0060	0.0055	154.7	0.0068
130	111.3	106.4	0.0048	0.0046	98.4	0.0042
200	84.2	84.0	0.0038	0.0037	56.9	0.0026
300	58.8	58.6	0.0029	0.0029	16.4	0.0008